A 3-D Finite Deformation Anisotropic Visco-Plasticity Model for Fiber Composites

H. D. ESPINOSA,* H-C. LU, P. D. ZAVATTIERI AND S. DWIVEDI
School of Aeronautics and Astronautics
Purdue University
West Lafayette, IN 47907-1282

ABSTRACT: A 3-D finite deformation anisotropic visco-plasticity model is presented for fiber composites in total Lagrangian co-ordinates. The plastic potential function is given by a quadratic function in stresses in the local co-ordinates system of the lamina. The model is used to derive the anisotropic plastic constitutive relation of a woven composite made of S-2 glass fibers embedded in polyester resin with approximately 60% by weight of fibers. The coefficients of the constitutive model are experimentally determined through off-axis tension tests and out-of-plane shear tests. Off-axis tension tests are carried out by varying the angle between the fiber orientation and loading direction. The measured stress-strain curves are used to derive a master effective stress–effective plastic strain curve, which is described by two power laws. A modified Arcan fixture is used to carry out pure shear tests to determine the out-of-plane shear coefficient. Compression tests are carried out to establish the material compressive response in the plane of the lamina and along the fiber direction. The anisotropic plasticity model is integrated into the in-house finite element code FEAP98. Numerical analyses are carried out for the off-axis tension tests and compression tests. These analyses show that the model reasonably predicts the constitutive response of woven GRP composites in confirmation with the experimental data. The model further incorporates strain rate and temperature dependence on the anisotropic plastic flow constitutive law. Ballistic penetration simulations are carried out using the integrated code. The velocity at the back surface of the composite target, obtained by analyses, is compared with the data measured experimentally using interferometry. Insight into the failure process is obtained through analysis of different energy dissipation mechanisms.

INTRODUCTION

FIBER REINFORCED PLASTIC (FRP) composite materials, especially the glass fiber reinforced plastic (GRP) composites, are potential materials for many ap-

---

*Author to whom correspondence should be addressed.

369

plications. Of special interest is their use in some crucial applications such as design of weight efficient aircrafts, submarines and armor vehicles. FRP materials in these applications are subjected to very large deformation at high strain rate leading to failure in various modes, (e.g., matrix cracking, delamination, fiber-matrix debonding, micro-buckling, fiber breakage, etc.). Comprehensive reviews on various failure modes in FRP materials under impact loading and influence of constituent materials, (viz., matrix, fiber and interphase) are given in Cantwell et al. [1] and Abrate [2,3]. During the on-going research of which the present work is a part, Espinosa et al. [4] have studied the penetration behavior of woven GRP composite, made of S-2 glass fibers embedded in a polyester resin matrix with approximately 60% fiber by volume, at normal impact velocities of 180–200 m/s. As shown in Figure 1, three distinct zones of damage can be observed, (viz., extensive delamination and fiber shearing in zone A, tensile fiber failure with large fiber deflection in zone B, and lastly fiber microfracture and buckling in zone C). The velocity history recorded at the GRP target plate free surface and conical steel projectile back surface are representative of the accumulative effect of the materials response in the presence of damage which will serve as an important validation
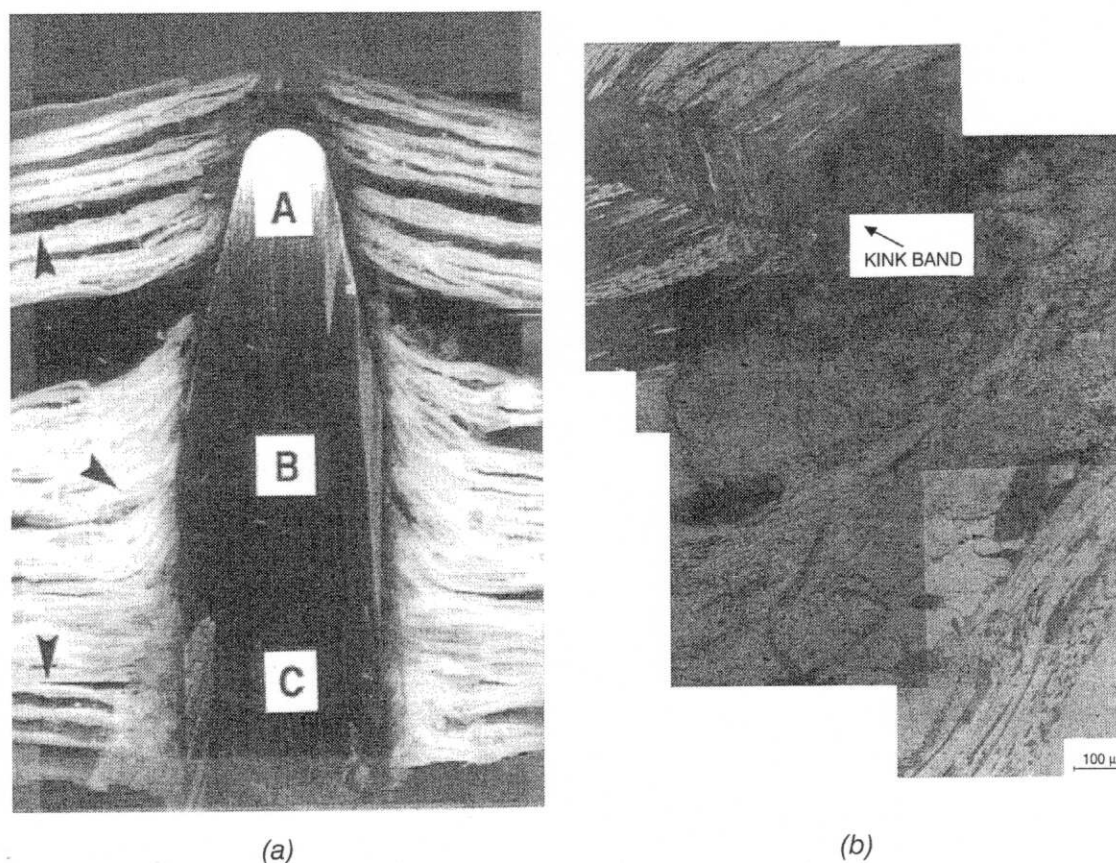

(a)   (b)

Figure 1. (a) Photograph of woven GRP sample recovered after penetration experiment. (b) Optical micrograph taken at the boundary between Regions A and B. Fiber kinking and matrix cracking are observed in 0° and 90° plies, respectively.

tool for future finite element modeling. Developing a representative finite element model to simulate a such complex response of FRP materials to impact loading is still a challenge. A three-dimensional finite deformation anisotropic visco-plastic constitutive model is proposed herein as a first step towards the development of the finite element model.

Numerous models have been proposed in the past to describe the anisotropic constitutive behavior of FRP materials before and after failure in the presence of damage. Sun and Chen [5] proposed a quadratic yield function and an associative flow rule based on Hill's anisotropic criteria [6] to describe the anisotropic plastic behavior of composite materials. By determining the constants of the yield function, they proposed that the anisotropic flow behavior of composite materials for different ply orientations can be described by a single curve in the effective stress–effective plastic strain space. Chen et al. [7] have extended the above yield function to account for the compressibility of the plastic deformation by introducing a plastic Poisson's ratio (PPR). They propose to carry out the tests for a particular material to determine the variation of effective stress with effective plastic strain under various loading conditions. The constants of the yield function are then determined so that these curves converge to a master effective stress–effective plastic strain curve.

O'Donoghue et al. [8] have used Hill's anisotropic yield function to describe the plastic flow of composite materials. The dependence of the pressure on the deviatoric strain components are taken into account by adding the appropriate terms in the equation of state of the material. Voyiadjis and Thiagarajan [9,10] have proposed an anisotropic yield surface model for directionally reinforced composite materials. In their model, the axial and shear strength parameters are combined through four tuning constants to arrive at a fourth order anisotropic yield tensor. The yield tensor is easy to implement in any finite element code either in local co-ordinates of the lamina or in the global co-ordinates through a second order co-ordinate transformation.

These yield functions provide the means to computationally homogenize the directional properties of composite materials. They allow a formulation applicable for such materials in general and amenable for easy implementation in a finite element computer program. In contrast, micromechanical models, Aboudi [11], Paley and Aboudi [12], Stout et al. [13], treat the matrix and fiber materials separately and derive the overall constitutive relation of a cell using periodicity and traction continuity at the boundary of sub-cells. On one hand, homogenized constitutive relations are simple to use in a finite element code but their capability to simulate extensive damage during impact and penetration remains questionable. On the other hand, micromechanical cell models can simulate such damage in detail, but they are highly computer intensive, applicable only to unidirectional composite and not viable for modeling some inherent characteristics of FRP materials, (e.g., waviness, see Hsiao and Daniel [14–16]).

In light of the above factors, a fully 3-D finite deformation anisotropic visco-plasticity model is proposed. The model parameters for a woven composite are determined through off-axis and shear experiments. The model has been integrated with the in-house version of the finite element code FEAP98. The integrated code has been used to analyze the off-axis tension tests and compression tests. The obtained results are in close agreement with the experimental results. The integrated code is further used to simulate the ballistic penetration experiments using more advanced feature of FEAP98, which combines the visco-plasticity model with contact/interface model and mesh adaptivity [17,18]. The visco-plasticity model is used to simulate inelasticity within each individual lamina accounting for fiber orientation, rate effects, and large deformation effects including large displacements and rotations of laminae. Interaction between laminae before and after delamination is analyzed using interface cohesive element (see Espinosa et al. [18]). Mesh adaptivity is used to resolve excessive mesh distortion at regions where there is large deformation. In addition, a complete analysis of energy dissipation is used to understand the failure process.

The following sections describe the plasticity model, experimental work, and results from analyses carried out with the anisotropic visco-plasticity model.

3-D FINITE DEFORMATION ANISOTROPIC PLASTICITY MODEL

Experiments performed on glass fiber composites show that failure occurs at strains of a few percent. However, the material undergoes very large displacement and rotation before and after delamination during impact and penetration, see Espinosa et al. [4]. Therefore, large deformation analyses of fiber composites can be carried out based on the assumption of large displacements and rotations, but small strains (about 2–3%) through appropriate finite deformation stress and strain measures. A three dimensional finite deformation anisotropic plasticity model is developed in total Lagrangian co-ordinates [19]. As shown in Figure 2, considering a solid with volume B_o in the reference configuration, and a deformation process characterized by the mapping $\mathbf{x}(\mathbf{X},t)$, a material point initially at $\mathbf{X}$ will be located at $\mathbf{x} = \mathbf{X} + \mathbf{u}$ after deformation, in which $\mathbf{u}$ is the displacement vector. A displacement based finite element formulation is obtained from the weak form of the momentum balance or dynamic principle of virtual work. The weak form at time t in total Lagrangian co-ordinates, (i.e., referred to the reference configuration), is given by

$$\int_{B_o} [\nabla_o \mathbf{T}^o + \rho_o (\mathbf{b}_o - \mathbf{a})] \cdot \eta dB_o = 0 \qquad (1)$$

$$\int_{B_o} \mathbf{T}^o : \nabla_o \mathbf{h} dB_o - \int_{B_o} \mathbf{r}_o (\mathbf{b}_o - \mathbf{a}) \cdot \mathbf{h} dB_o - \int_{S_{o\sigma}} \mathbf{t} \cdot \mathbf{h} dS_o = 0 \qquad (2)$$
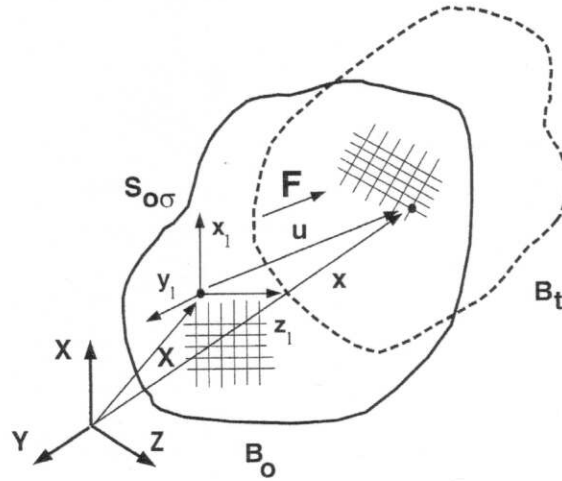
Figure 2. *Total Lagrangian continuum model.*

where $\mathbf{T}^o$ is the first Piola-Kirchhoff stress tensor at time t; $\mathbf{b}_o$, $\mathbf{a}$, and $\mathbf{t}$ are the body force vector, acceleration vector, and boundary traction vector on volume B_o and boundary $S_{o\sigma}$, respectively. Virtual displacement field η is assumed to be admissible, and ρ_o represents the material density per unit volume in the reference configuration. The symbol ∇_o denotes the material gradient with respect to the reference configuration, and ":" is used to denote the inner product between second order tensors, e.g., $\mathbf{A} : \mathbf{B} \equiv A_{ij} B_{ji}$, where the summation convention on repeated indices is implied.

Alternately, the weak form of the momentum balance, in terms of spatial quantities, is given by

$$\int_{B_o} \tau : \nabla^s \eta \, dB_o - \int_{B_o} \rho_o (\mathbf{b}_o - \mathbf{a}) \cdot \eta \, dB_o - \int_{S_{o\sigma}} \mathbf{t} \cdot \eta \, dS_o = 0 \tag{3}$$

in which superscript s stands for the symmetric part of the tensor, $\tau = \mathbf{F}\mathbf{T}^o$ is the Kirchhoff stress, $\mathbf{F}$ is the deformation gradient at time t, and ∇ is the spatial deformation tensor. As Equation (3) shows, the equation of motion in its weak form states that the work done by the stresses τ over strains $\nabla^s \eta$ equals the work done by applied body forces, inertia forces, and surface tractions.

In the absence of body forces, the above equation can be written at time t for explicit integration as,

$$\mathbf{M}\mathbf{a} = \mathbf{f}_{\text{ext}} - \mathbf{f}_{\text{int}} \tag{4}$$

where $\mathbf{M}$ is the lumped mass matrix, $\mathbf{a}$ is the global acceleration vector and $\mathbf{f}_{\text{ext}}$ and $\mathbf{f}_{\text{int}}$ are the external and internal force vectors. In order to obtain a uniform mass distribution in the mesh, the element mass was lumped proportional to the angles formed by the corner nodes and midnodes, as detailed in Reference [17].

The constitutive response of the GRP composite is formulated in terms of the Green-Lagrange strain tensor $\mathbf{E}$ and the work conjugate second Piola-Kirchhoff stress tensor $\mathbf{S}$ [19]. The Green Lagrange strain rate tensor at time step $t + \Delta t$, is given as,

$$\dot{E}_{ij} = \frac{1}{2\Delta t}[(F_{ki}F_{jk})_{t+\Delta t} - (F_{ki}F_{jk})_t] \tag{5}$$

where F_{ij} is the ij components of deformation gradient and Δt is the incremental time step. All quantities in the above equation are defined in the global co-ordinates $(\mathbf{X},\mathbf{Y},\mathbf{Z})$. Since the second Piola Kirchhoff stress tensor and the Green Lagrange strain tensor are energy conjugate and independent of rigid body motions, any material description developed for infinitesimal displacement analysis, using engineering stress and strain measures, can be directly extended for large displacement and rotation but small strains analyses.

Accordingly, the rate form of the elastic constitutive law, assuming a hyperelastic material, is given by

$$\dot{S}_{ij} = C_{ijkl}\dot{E}^e_{kl} \tag{6}$$

where $\mathbf{C}$ is the elastic anisotropic composite material stiffness tensor in the global co-ordinates, and $\dot{\mathbf{E}}^e$ is the elastic component of the Green Lagrange strain rate tensor. As given in Reference [17], the Kirchhoff stress τ and second Piola-Kirchhoff stress $\mathbf{S}$ are related through the relation $\tau = \mathbf{FSF}^T$. In the case of anisotropic composite materials, the elastic constitutive matrix C_{IJKL} is defined in the local co-ordinate system of the lamina $(\mathbf{x}_l,\mathbf{y}_l,\mathbf{z}_l)$. The constitutive matrix C_{ijkl} is obtained by the standard transformation law [20] $C_{ijkl} = \mathbf{T}_{iI}\,\mathbf{T}_{jJ}\,\mathbf{T}_{kK}\,\mathbf{T}_{lL}\,C_{IJKL}$, where $\mathbf{T}$ is the transformation matrix between the global coordinate and the local coordinate.

The elastic components of the strain rate tensor are obtained from an additive decomposition of the total strain rate, namely,

$$\dot{E}^e_{ij} = \dot{E}_{ij} - \dot{E}^p_{ij} \tag{7}$$

In the above equation, $\dot{E}^p_{ij}$ is the plastic strain rate which is given by the flow rule as,

$$\dot{E}^p_{ij} = \dot{\lambda}\frac{\partial f}{\partial S_{ij}} \tag{8}$$

Here, f is the plastic flow potential and $\dot{\lambda}$ is the plastic rate proportionality factor. The inelastic behavior of the composite is modeled based on the small deformation yield function, quadratic in stresses, proposed by Hill [5] and later adopted by Sun and Chen [5], namely,

$$2f(S_{ij}) = a_{11}S_{11}^2 + a_{22}S_{22}^2 + a_{33}S_{33}^2$$

$$+ 2a_{12}S_{11}S_{22} + 2a_{13}S_{11}S_{33} + 2a_{23}S_{33}S_{22}$$

$$+ 2a_{44}S_{23}^2 + 2a_{55}S_{13}^2 + 2a_{66}S_{12}^2 \tag{9}$$

Experimental observations show that glass fiber composites behave linearly up to failure if the load is applied in the fiber direction. Hence, for orthogonal fibers oriented along direction 1 and 2, it is assumed that $E_{11}^p = E_{22}^p = 0$. The above flow potential then reduces to,

$$f(S_{ij}) = \frac{1}{2}(S_{33}^2 + a_{44}S_{23}^2 + a_{55}S_{13}^2 + a_{66}S_{12}^2) \tag{10}$$

For equal fiber volume fractions in the principal 1 and 2 directions, $a_{44} = a_{55}$ is obtained which further reduces the yield function to,

$$f(S_{ij}) = \frac{1}{2}[S_{33}^2 + a_{44}(S_{23}^2 + S_{13}^2) + a_{66}S_{12}^2] \tag{11}$$

Defining an effective stress as,

$$\overline{S} = \sqrt{3f} \tag{12}$$

and using the flow rule given above with the assumption of identical behavior in tension and compression, the rate of plastic work is obtained from Equations (9) to (12) as,

$$\dot{W}^p = S_{ij}\dot{E}_{ij}^p = \overline{S}\dot{\overline{E}}^p \tag{13}$$

The proportionality factor of Equation (8) is given by,

$$\dot{\lambda} = \frac{3\dot{\overline{E}}^p}{2\overline{S}} \tag{14}$$

where $\dot{\overline{E}}^p$ is the effective plastic strain rate. The effect of strain rate and temperature is modeled by defining the material strength in terms of an effective stress which includes temperature and strain rate terms, viz.,

$$\dot{\overline{E}}^p = \dot{\overline{E}}_o^p \left[\frac{\overline{S}}{g(\overline{E}^p, T)} \right]^m \quad \text{if } \overline{S} > g(\overline{E}^p, T) \tag{15}$$

$$g(\bar{E}^p, T) = \bar{S}_y \left[1 - \left(\frac{T - T_o}{T_m - T_o} \right)^\alpha \right] \qquad (16)$$

in which $\bar{S}_y$ is the flow stress at reference plastic strain rate $\dot{\bar{E}}_o^p$ and temperature T_o. T_m is the maximum temperature at which the FRP material loses its strength. $\bar{S}$ is the flow stress at current plastic strain rate $\dot{E}^p$ and temperature T, m and α are the rate and temperature sensitivity exponents, respectively. The reference flow stress $\bar{S}_y$ is defined by an experimentally found power law, viz.,

$$\bar{S}_y = \left(\frac{\bar{E}^p}{A} \right)^{1/n} ; \; \bar{E}^p = A(\bar{S}_y)^n \qquad (17)$$

in which n is the strain hardening exponent. A summary of the constitutive equations, in discrete form are given in Table 1.

It should be noted that depending on the matrix material, other functional forms for the description of inelasticity may be needed. For instance, visco-elastic representations would be equally feasible. For the purpose of simulating ballistic penetration of GRP composites, we assume that a visco-plastic description can adequately capture the GRP material response in a macroscopic sense, i.e., ply inelasticity (matrix cracking, fiber debonding, matrix inelasticity) is represented

Table 1. Summary of constitutive equations in discrete form.

$$\dot{S}_{t+\Delta t} = C\dot{E}_{t+\Delta t}^e$$

$$\dot{E}_{t+\Delta t} = \dot{E}_{t+\Delta t}^e + \dot{E}_{t+\Delta t}^p$$

$$\dot{E}_{t+\Delta t}^p = \lambda \frac{\partial f}{\partial S_{t+\Delta t}} = \frac{3\dot{\bar{E}}^p}{2\bar{S}} \frac{\partial f}{\partial S_{t+\Delta t}} = \dot{\bar{E}}_{t+\Delta t}^p N_{t+\Delta t}$$

$$N_{t+\Delta t} = \frac{3}{2} \frac{\partial f}{\partial S_{t+\Delta t}} \frac{3}{\bar{S}_{t+\Delta t}} = \frac{3}{2\bar{S}} \begin{bmatrix} 0 & 2a_{66}S_{12} & 2a_{55}S_{13} \\ 2a_{66}S_{12} & 0 & 2a_{44}S_{23} \\ 2a_{55}S_{13} & 2a_{44}S_{23} & S_{33} \end{bmatrix}_{t+\Delta t}$$

$$\bar{S}_{t+\Delta t} = \sqrt{3f_{t+\Delta t}(S_{ij})_{t+\Delta t}}$$

$$g(\bar{E}_{t+\Delta t}^p, T) = \bar{S}_{y,t+\Delta t} \left[1 - \left(\frac{T - T_o}{T_m - T_o} \right)^\alpha \right]$$

$$\bar{S}_{y,t+\Delta t} = \left(\frac{\bar{E}_{t+\Delta t}^p}{A} \right)^{\frac{1}{n}}$$

$$\dot{\bar{E}}_{t+\Delta t}^p = \dot{\bar{E}}_o^p \left[\frac{\bar{S}_{t+\Delta t}}{g(\bar{E}_{t+\Delta t}^p, T)} \right]^m$$

by the model described in this section, while interply delamination is modeled by means of cohesive/contact laws.

EXPERIMENTAL DETERMINATION OF THE VISCO-PLASTICITY MODEL PARAMETERS

The anisotropic yield function given in Equation (11) involves two coefficients which need to be determined experimentally. Following Sun and Chen [5], the value of coefficient a_{66} is examined by carrying out off-axis tension tests and deriving a master effective stress-effective plastic strain curve. Coefficient a_{44} is determined by carrying out out-of-plane shear tests with Arcan's fixture. Compression tests in the thickness direction are carried out to study the effect of S_{33} in the yield function. Compression tests are also performed to examine the tensile vis-a-vis compressive response in the plane of lamina. The following subsections describe the off-axis tension tests, compression tests and Arcan's shear tests carried out to parameterize the visco-plasticity model. Experimental work related to determination of high strain rate and temperature effects parameters are the subject of future research work.

Off-Axis Tension Tests

The off-axis tension tests are carried out to examine the tensile response of the woven composite in the plane of lamina and derive the in-plane shear coefficient a_{66} from the test results. Figure 3 shows the schematic of the off-axis test specimen. Let S_x be the load applied in the plane of the lamina along the uniaxial direction X which makes an angle θ with respect to the fiber direction X_1. Axes 1, 2 and 3 are defined as material principal axes.

The stress components referred to these axes are,

$$S_{11} = \cos^2 \theta S_x$$

$$S_{22} = \sin^2 \theta S_x \tag{18}$$

$$S_{12} = -\sin\theta \cos\theta S_x$$

For the case of 2-D plane stress parallel to the X_1–X_2 plane, the plastic potential function given by Equation (11) reduces to,

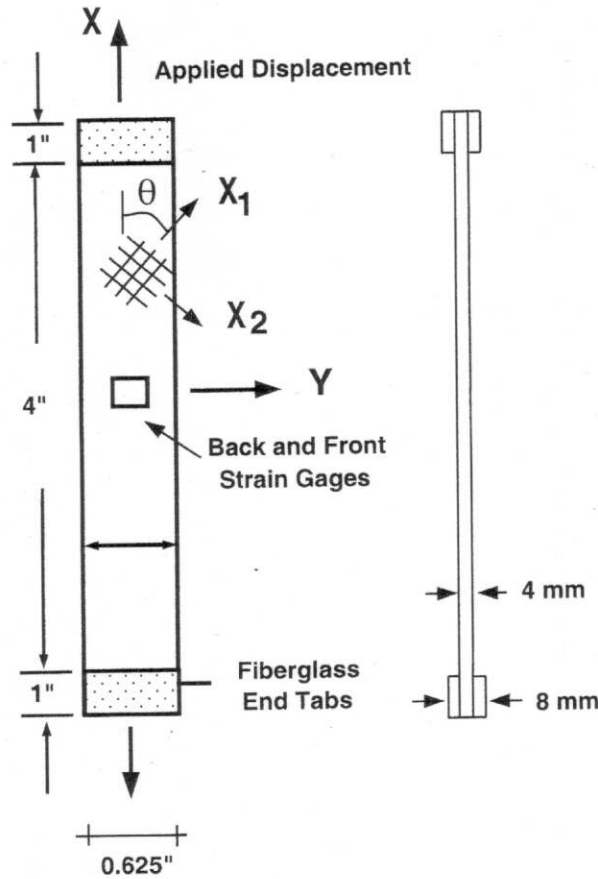$$f(S_{ij}) = a_{66} S_{12}^2 \tag{19}$$

Figure 3. *Off-axis tensile test specimen.*

Substituting the above equation into the effective stress equation, the effective stress can be derived in terms of the applied stress S_x and the fiber direction θ, namely,

$$\bar{S} = \sqrt{3a_{66} \cos^2\theta \sin^2\theta}\, S_x = h(\theta)S_x \tag{20}$$

where, $h(\theta) = \sqrt{3a_{66} \cos^2\theta \sin^2\theta}$ is a function of the fiber orientation θ.

The relationship between the incremental plastic strain and stress in terms of the applied state of stress reduces to,

$$\bar{\dot{E}}^p = \frac{2}{3}\bar{S}\dot{\lambda} = \frac{2}{3}h(\theta)S_x\dot{\lambda} \tag{21}$$

The inelastic strain components are derived by substituting the yield function into the flow equation, viz.,

$$\begin{bmatrix} \dot{E}_{11}^p \\ \dot{E}_{22}^p \\ 2\dot{E}_{12}^p \end{bmatrix} = \begin{bmatrix} 0 \\ 0 \\ 2a_{66}S_{12}\dot{\lambda} \end{bmatrix} \tag{22}$$

Using coordinate transformations, the equation for the strain in the X direction can be derived as,

$$\dot{E}_x^p = \cos^2\theta\,\dot{E}_{11}^p + \sin^2\theta\,\dot{E}_{22}^p - 2\cos\theta\,\sin\theta\,\dot{E}_{12}^p$$

$$= 2a_{66}\cos\theta\,\sin\theta\,S_x\dot{\lambda} = \frac{2}{3}h^2(\theta)S_x\dot{\lambda} \tag{23}$$

Comparing the above equation with the equation of the effective strain, the relationship between the effective strain rate and the plastic strain rate component in the X direction is obtained as,

$$\bar{\dot{E}}^p = \frac{\dot{E}_x^p}{h(\theta)} \tag{24}$$

Integrating both sides, the relation between the plastic strain in the X direction and the effective plastic strain can be obtained, viz.,

$$\bar{E}^p = \frac{E_x^p}{h(\theta)} \tag{25}$$

The above equations provide a useful relation to characterize the ratio between effective stress and effective plastic strain.

$$\frac{\bar{S}}{\bar{E}^p} = h^2(\theta)\frac{S_x}{E_x^p} \tag{26}$$

Hence, determining the variation of S_x vs. E_x^p experimentally, the master effective stress vs. effective plastic strain curve, $\bar{S}$ vs. $\bar{E}^p$, is obtained from the above relation.

Monotonic tension tests are performed on GRP off-axis specimens, shown in Figure 3, at different loading rates. Off-axis specimens are sliced from 1-inch thick GRP panels, then cut into different angles with a water-jet cutting machine. Fiberglass end tabs are bonded with epoxy to the specimen ends. These end tabs are strain compatible so as to avoid damage by gripping on the samples.

The experiments are conducted with an MTS servo-hydraulic machine controlled by an Instron 8500 controller which prescribes a constant displacement rate in order to simulate a constant strain rate experiment. Back-to-back axial strain gauges (micro-measurement EA-13-125AC-350) are mounted at the center of the specimens to measure the strains. The back-to-back mounting helps to examine bending effects during loading. A hydraulic grip is first applied to the end tabs and

the grips are aligned so that the longitudinal axis of the specimen coincides with the direction of the applied load in the plane of the specimen. The test specimens are held in such a way that sufficient lateral pressure is applied to prevent slippage between the grip face and the tabs.

Experiments are carried out at five different values of angle θ between zero and 45°. The displacement loading rate is varied as 0.001 mm/s and 0.1 mm/s. Results obtained show that thermoplastic composites do not have a well-defined yield point so that the master effective stress-effective plastic strain curve is described by a set of two power laws. The experimental results, master curve and the power law coefficients obtained by curve fitting are given in the next section.

Compression Tests

The response of the woven GRP composite in compression is determined experimentally by applying a compressive load in the plane of the lamina, as well as normal to the plane, i.e., in the thickness direction. Experiments are carried out with test specimens of 8 mm × 8 mm cross-section. Three different heights as 8 mm, 20 mm and 40 mm of the specimen are considered. The compression loading is applied in a MTS machine through a flat end indenter. A load alignment device is used to ensure that the load is uniformly distributed across both contact surfaces. When carrying out the experiments in the plane of the lamina, the load is applied at 0° and 45°, with the fiber directions to maintain loading symmetry. The displacement rate in all the experiments is kept as 0.001 mm/s. The strain gauge signals are measured with a Wheatstone Bridge and amplifier. The amplifier is set at a fixed gain of 100. Three experimental parameters, viz., displacement, load, and strain are recorded in a PC using the software LABVIEW.

Pure-Shear Tests

Coefficient a_{44} in the plastic yield potential is related to the out-of-plane shearing behavior of the composite. Its value can in principle be identified from pure shear loading obtained with an Arcan loading fixture, Arcan et al. [21–24], see Figure 4.

The plastic potential function for a pure shear test in the **1–3** direction reduces to

$$f(S_{ij}) = a_{44}S_{13}^2 \tag{27}$$

Using the definition of effective stress, the relation between the effective stress and applied stress can be found as,

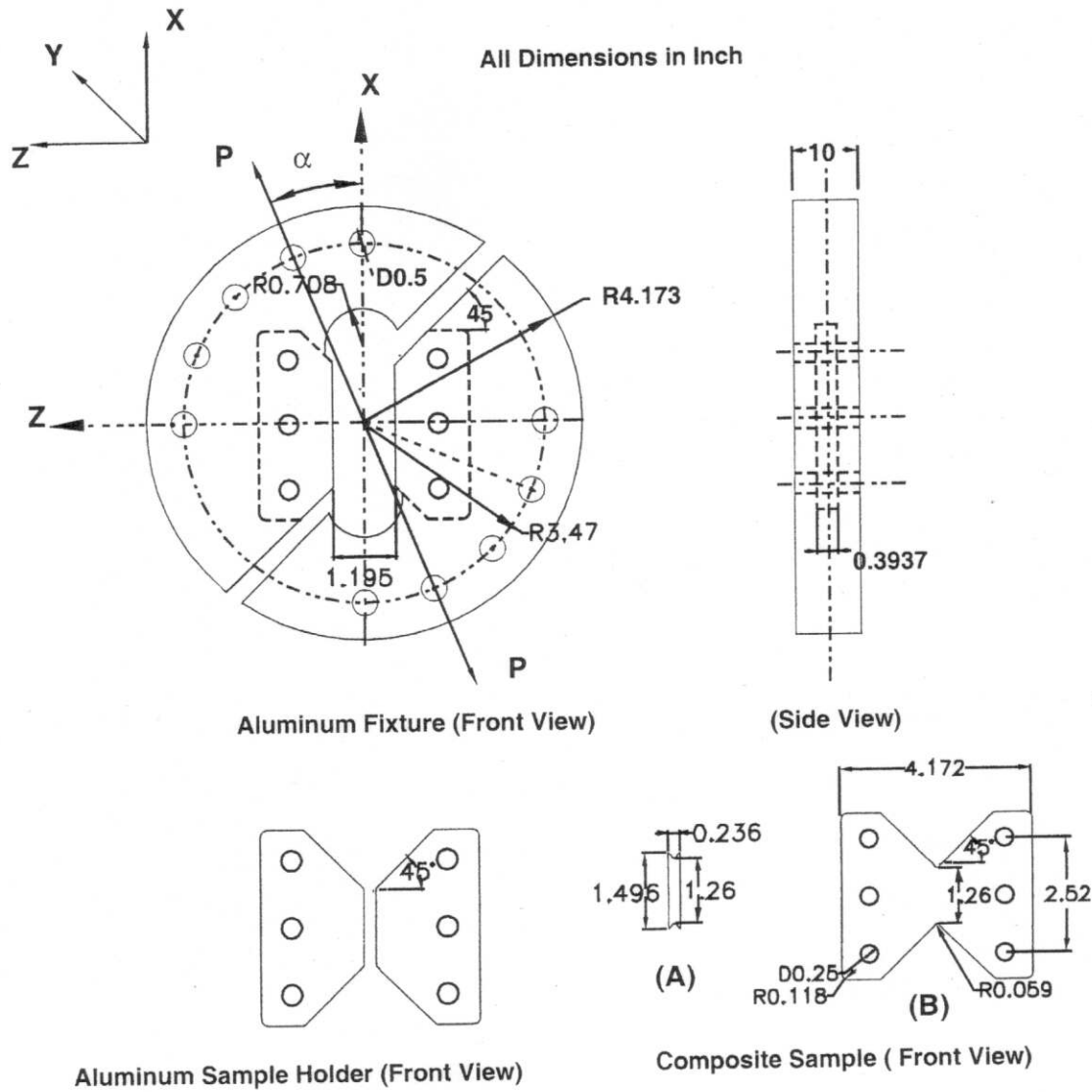$$\bar{S} = \sqrt{3a_{44}}\,S_{xz} = \sqrt{3a_{44}}\,S_{13} \tag{28}$$

All Dimensions in Inch

Aluminum Fixture (Front View)   (Side View)

Aluminum Sample Holder (Front View)   Composite Sample (Front View)

Figure 4. *Arcan's fixture for shear loading, Arcan et al., 1978.*

Applying the flow rule, the strain component in the **1–3** principal materials directions can be calculated in terms of the applied stress S_{xz}, viz.,

$$\dot{E}_{13}^p = 2a_{44}S_{13}\dot{\lambda} \tag{29}$$

with

$$\dot{\lambda} = \frac{\dot{E}_{13}^p}{2a_{44}S_{13}} \tag{30}$$

The effective plastic strain rate is related to the strain component S_{13} by the expression,

$$\bar{\dot{E}}^p = \frac{2}{3}\bar{S}\dot{\lambda} = \frac{\dot{E}_{13}}{\sqrt{3a_{44}}} \tag{31}$$

Hence, the relationship between the effective plastic strain and the experimentally measured strain can be found to be,

$$\bar{E}^p = \frac{E_{13}}{\sqrt{3a_{44}}} \tag{32}$$

The stress and strain relation between the effective values and experimental values can thus be built as

$$\frac{\bar{S}}{\bar{E}^p} = \frac{3a_{44}S_{13}}{E_{13}^p} \tag{33}$$

Having determined the master effective stress $\bar{S}$ vs. effective plastic strain $\bar{E}^p$ curve through off-axis tension tests, coefficient a_{44} is easily determined from the above equation. Hence, a unified visco-plasticity law is defined in terms of effective stress and strain measures.

Experiments are carried out with the modified Arcan fixture shown in Figure 4. A salient feature of the modified fixture is the two piece butterfly shaped Aluminum holder as shown in Figure 4. GRP specimen sample A is glued to the holder with FM-1000 (from Cytex company) by placing the film and specimen into a hot oven. The oven is heated to 175°C within an hour then kept at this constant temperature for another hour. The assembled holder fits concentrically into the fixture to avoid any eccentricity during loading. It is mounted into the Arcan fixture by 0.25-inch screws that transfer the load to the specimen through the plate. The load is applied to the fixture at an angle α with respect to the **X**-direction. Arcan's fixture is connected to the testing machine by means of pins. These pins allow the rotation of the fixture to avoid load misalignments. In order to ease the constraint of mounting the small size specimen, A in Figure 4, to the Aluminum holder, a GRP butterfly specimen, B in Figure 4, is designed to fit directly into Arcan's fixture without the need of the Aluminum holder.

Pure-shear experiments are conducted with an MTS servo-hydraulic system, applying the load with an angle $\alpha = 0$. Three parameters, viz., displacement, load, and strain are recorded by a PC with LABVIEW. The tests are performed under displacement control with a displacement rate set at 0.001 mm/sec. Back-to-back rosette strain gauges (WA-06-125-120) are mounted to measure the strain histories. These strain gauges are bonded-wired-type gauges with a resistance of 120 Ω. The back-to-back strain gauges help to identify any bending effect. The experimental results obtained from pure-shear and compression-shear tests are given in the following sections.

EXPERIMENTAL RESULTS

Various off-axis tension tests, compression tests and pure-shear tests carried out are summarized in Table 2. The experimental results, master effective stress-effective plastic strain curve and the values of the parameters are described below.

Off-Axis Tension Tests

The off-axis tension tests are carried out with five values of θ, viz., 0°, 10°, 20°, 30°, and 45°, and at two displacement loading rates of 0.001 mm/s and 0.1 mm/s. The gauge length of 100 mm of the specimen gives the strain rate of 10^{-5} and 10^{-3}/sec, respectively. The tensile load is applied monotonically until failure, if any, or until no appreciable change in the load is observed indicating the onset of perfectly inelastic flow. In the case of θ equal to 20°, the loading direction is reversed after entering into the plastic regime to test the materials behavior during unloading. The stress-strain curves obtained from experiments at a strain rate of 10^{-5}/sec are shown in Figure 5. The figure shows that the material behaves elastically when the load is applied along the fiber direction, i.e., $\theta = 0°$ and $\theta = 90°$. This justifies neglecting the S_{11} and S_{22} stress components from the plastic potential function, Equation (10). As θ increases, the degree of plasticity exhibited by the material also increases. Maximum plasticity is observed at $\theta = 45°$ degrees. It is noticed that the material behaves non-linearly from the beginning of the loading. Moreover, it exhibits non-linear behavior during unloading as well. As shown in Figure 5, $\theta = 20°$, complete unloading results in an irreversible strain.

The variation of effective stress $\bar{S}$ with effective plastic strain $\bar{E}^p$ is obtained from the experimental data for various values of θ using Equation (26). The master effective stress—effective plastic strain curve so obtained is shown in Figure 6. As the material exhibits non-linearity from the beginning of the loading phase, the master curve is described through two power laws, whose coefficients are obtained as, $A = 3.55 \cdot 10^{-28}$ and $n = 3.28$ if $\bar{E}^p \leq 0.72\%$, and $A = 3.55 \cdot 10^{-55}$ and $n = 6.78$, otherwise.

Figure 7 shows the stress-strain curves for θ equal to 10° and 30° determined experimentally at the two strain rates of 10^{-5} and 10^{-3}/sec. It can be seen that the material does not show considerable rate sensitivity at strain rates below 10^{-3}/sec.

Compression Tests

Compression tests with loading in the plane of lamina were conducted, on samples with fiber orientations of 0° and 45° with respect to the loading direction, at a displacement rate of 0.001 mm/sec. In order to minimize the end effect due to inclined fibers and obtain pure compressive loading at the center of specimen, several height to width ratios are considered in the case of 45° orientation. However,

Table 2. Summary of quasi-static experiments.

| Experiment Number	Mode	Fiber Orientation vs. Loading Direction	Specimen Dimensions (Width × Height × Thickness) [mm] × [mm] × [mm]	Cross Sectional Area [mm × mm]	Displacement Rate [mm/sec]
T-00-01	Off-Axis Tension	0°	15.9 × 100.8 × 4.2	67.1	10^{-4}
T-00-01	Off-Axis Tension	0°	15.9 × 99.7 × 4.2	67.0	10^{-4}
T-00-01	Off-Axis Tension	10°	15.9 × 100.3 × 4.3	67.7	10^{-2}
T-10-02	Off-Axis Tension	10°	16.52 × 101.7 × 1.1	18.6	10^{-2}
T-10-03	Off-Axis Tension	10°	16.47 × 101.4 × 1.1	18.3	10^{-4}
T-20-01	Off-Axis Tension	20°	15.9 × 100.7 × 4.3	67.6	10^{-2}
T-20-02	Off-Axis Tension	20°	16.59 × 101.88 × 1.2	19.9	10^{-4}
T-30-01	Off-Axis Tension	30°	15.9 × 101.4 × 4.3	67.62	10^{-2}
T-30-02	Off-Axis Tension	30°	16.5 × 101.1 × 1.14	18.8	10^{-2}
T-30-03	Off-Axis Tension	30°	16.6 × 101.8 × 1.1	17.4	10^{-4}
T-45-01	Off-Axis Tension	45°	16.5 × 100.5 × 1.2	19.8	10^{-2}
T-45-02	Off-Axis Tension	45°	16.15 × 101.2 × 1.25	20.19	10^{-4}
C-00-01	Compression	0°	8.07 × 8.04 × 8.02	64.72	10^{-2}
C-00-02	Compression	0°	8.06 × 8.07 × 8.03	64.72	10^{-4}
C-45-01	Compression	45°	8.03 × 7.99 × 7.99	64	10^{-2}
C-45-02	Compression	45°	8.03 × 19.85 × 8.05	64.6	10^{-2}
C-45-03	Compression	45°	7.47 × 39.54 × 7.47	55.8	10^{-4}
C-45-04	Compression	45°	7.47 × 39.54 × 7.47	55.8	10^{-4}
C-Z-01	Compression	Z Direction	7.88 × 8.01 × 7.98	62.9	10^{-2}
C-Z-02	Compression	Z Direction	8.03 × 20.09 × 8.05	64.64	10^{-2}
PS-00-01	Pure Shear	0°	6 × 31.77 × 9.98	317.06	10^{-4}
PS-00-02	Pure Shear	0°	5.98 × 32.35 × 9.98	322.85	10^{-4}
PS-00-03	Pure Shear	0°	106 × 33.78 × 9.97	336.78	10^{-4}
PS-00-04	Pure Shear	0°	106 × 33.78 × 9.97	336.78	10^{-4}
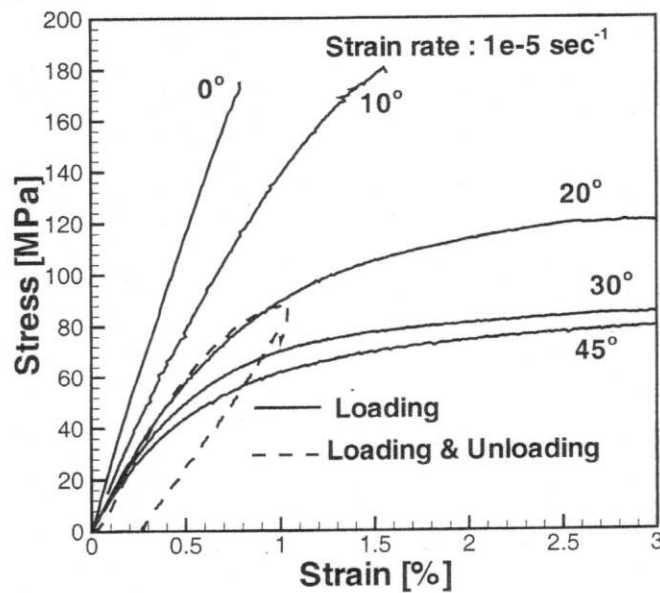
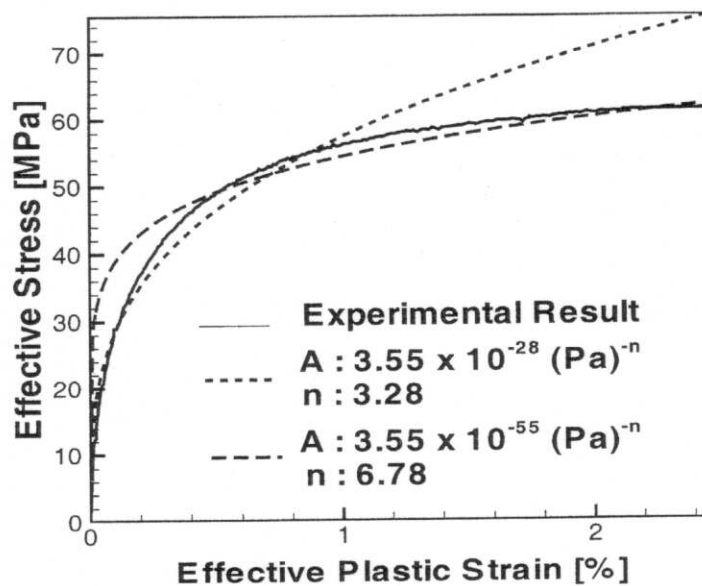**Figure 5.** *Experimental stress-strain curves from off-axis tension tests.*

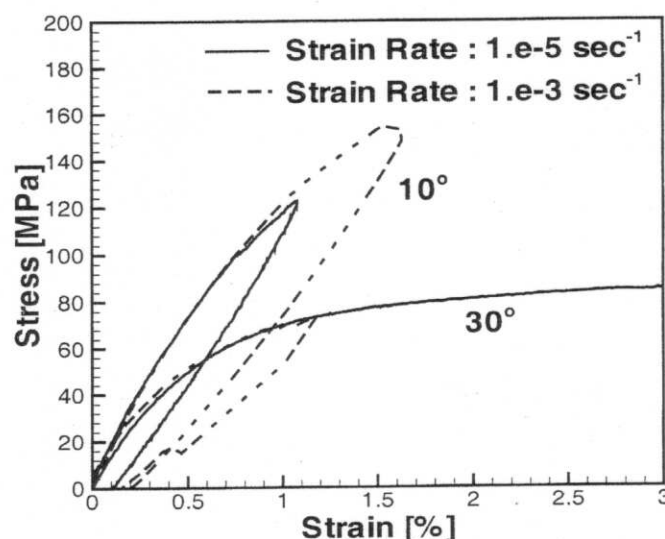**Figure 6.** *Effective stress vs. effective plastic strain curve and power law fit.*

Figure 7. *Experimental stress-strain curves from off-axis loading/unloading tension tests.*

due to absence of such end effects in the case of 0° orientation, the specimen height is kept equal to the width in this case.

The stress-strain curve for the 45° fiber orientation is shown in Figure 8 together with the tension test result for the same orientation. It is observed that the material response under compression is also non-linear from the beginning of the loading. As the height to width ratio increases, the compressive stress-strain curve converges towards the stress-strain curve obtained by the off-axis tension test for the same fiber orientation.

The stress-strain curves under compression loading along the fiber direction, i.e., 0°, obtained at the two loading rates of 0.001 mm/sec and 0.1 mm/sec are shown in Figure 9. The result obtained from the off-axis tension test for the same fiber orientation is also shown in the figure. For the gauge length of 8 mm, the two loading rates give the strain rates of $1.25 \cdot 10^{-4}$ and $1.25 \cdot 10^{-2}$/sec. It is observed that the material does not have significant rate dependence at the tested strain rates. During monotonic loading at both loading rates, the stress increases linearly except for the outset of loading. The lack of linearity at the early stages of loading is due to the evolution of the contact traction rather than a true material behavior. A nonuniform contact pressure is expected from the material heterogeneity and fiber waviness. The linear increase gives a Young's modulus of 22 GPa, which is very close to the one obtained by Chou et al. [25] using ultrasonic wave measurement technique. A sudden relaxation in stress occurs after reaching the maximum stress of 190 MPa. This is typical of material instability leading to buckling of the glass fibers and delamination of the specimen. A secondary increase in stress is observed which shows that the material still possesses resistance after fiber buckling. Delamination and other failure mechanisms accumulate reducing the stress further. The post buckling behavior is different for the two different displacement
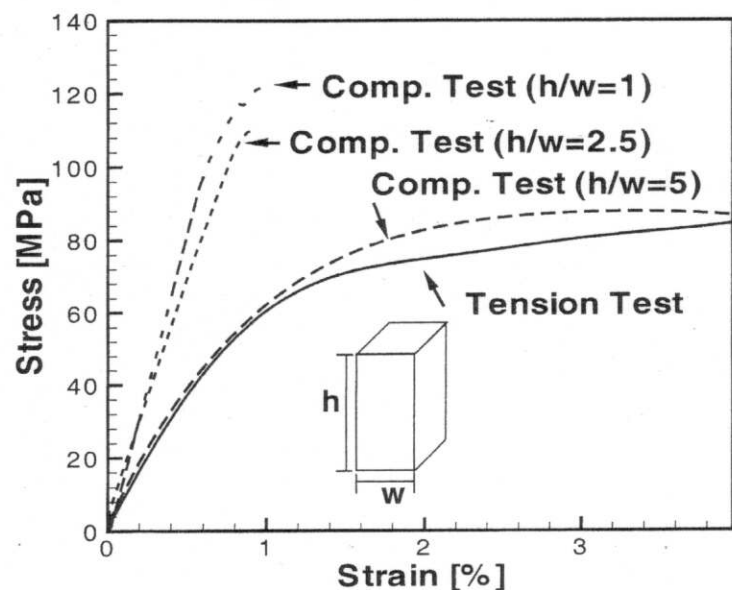
Figure 8. *Stress-strain curves from tension and compression off-axis experiments. Fiber orientation at 45°.*
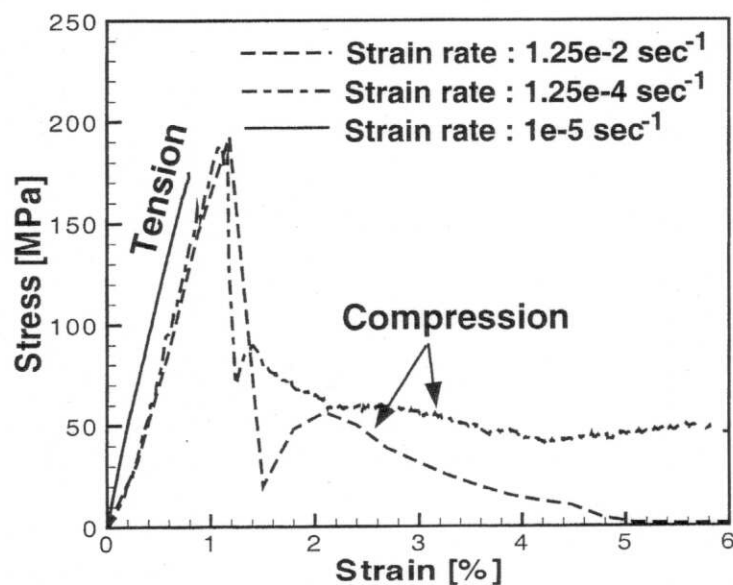

Figure 9. *Stress-strain curves on 0° fiber-orientation from compression experiments at two different strain rates.*
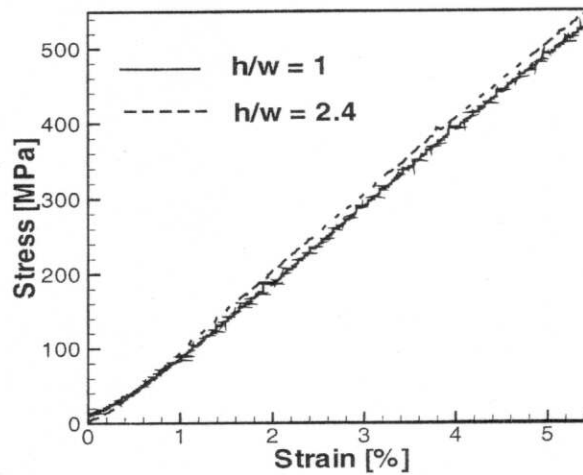
Figure 10. Stress-strain curves from compression tests on the Z-direction.

loading rates. The secondary peak stress value is 95 MPa and 60 MPa for the loading rates of 0.001 mm/s and 0.1 mm/s, respectively. Similarly, the stress reduces to 50 MPa and 10 MPa at a strain of 5 %. It is observed from Figures 8 and 9 that the response of the tested composite material, in tension and compression, is approximately identical before buckling. The differences observed are within experimental tolerance and may be neglected.

Figure 10 shows the experimental stress-strain curve obtained from compression tests when the load is applied normal to the plane of the lamina. Experiments have been carried out with specimen height of 8 mm and 20 mm. The load is applied monotonically until failure. It is observed that the stress-strain curve obtained with the two specimen lengths matches within the experimental tolerance. The test results show that the material response is linear, until failure, under compression along the matrix direction. Based on this experimental observation, the plastic potential function, Equation (11) is further modified by eliminating the S_{33} term, i.e.,

$$f(S_{ij}) = a_{44}(S_{23}^3 + S_{13}^2) + a_{66}S_{12}^2 \tag{34}$$

Pure-Shear Tests

Out-of-plane shear and compression-shear quasi-static tests were conducted using Arcan's fixture, see Figure 4. The pure-shear tests were conducted by applying the load along the X axis in order to identify the shear modulus, C_{13}, as well as the out-of-plane shear parameter used in the anisotropic flow potential function. In the first set of experiments, test specimen A is used which is mounted on the Aluminum sample holder. In the second set of experiments, specimen B is used which is
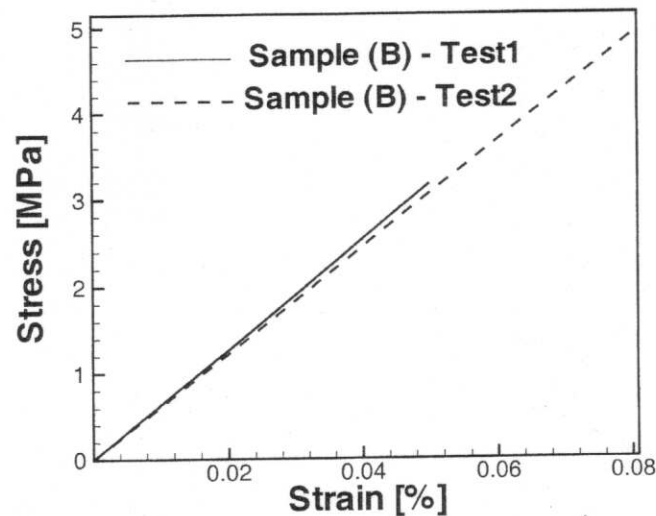
Figure 11. *Stress-strain curve from pure-shear experiment.*

directly mounted on the fixture. The stress-strain curves obtained experimentally, with specimen (B), are shown in Figure 11. Only specimen B exhibited the desired repeatability of experimental results.

The stress-strain $(\tau - \gamma)$ curve shows an inelastic material behavior, under quasi-static loading, in view that the tangent slope observed in Figure 11 is smaller than the shear modulus of 9.75 GPa, obtained at the U.S. Army Research Laboratory [25] by means of ultrasonic wave measurement. Therefore, it appears that a not-well defined yield point exists as previously observed in the off-axis experiments. The important feature to note is that the material failed in out-of-plane shear at extremely small strains. For the sample B tests, the composite broke along a line connecting screws directly on the composite sample. This is believed to be the result of defects introduced during the drilling process. The force transferred through the specimen central cross-section, where the strain was measured by rosette strain gauges, still represents a true material property.

According to the modified flow potential, Equation (34), a_{44} and a_{66} are the only parameters in the model. One of these parameters is arbitrary because the potential is defined up to a constant. The other coefficient needs to be identified from a multi-axial test involving all the stress components appearing in the flow potential. Since one of the objectives in the modeling is to define a master curve in the effective stress–effective plastic strain plane, a_{44} is here determined from Equation (33). Selecting $a_{66} = 1$, the value of a_{44} is chosen so that the effective stress-effective plastic strain curve from out-of-plane pure shear matches with the master effective stress-effective plastic strain curve. Figure 12 shows the curves obtained with $a_{44} = 0.5$, 1.0 and 2.0. The zoomed region in Figure 12 shows a reasonable match between the measured shear curve and the master curve when $a_{44} = 1.0$. Thus for this particular woven composite, both parameters a_{44} and a_{66} are adopted to be unity through the numerical simulations.
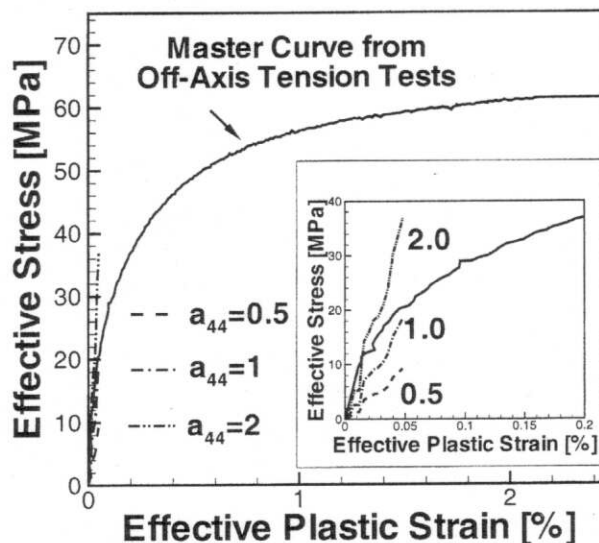
Figure 12. Stress-strain curve from pure-shear experiment.

NUMERICAL SIMULATIONS

The 3-D finite deformation anisotropic plasticity model is integrated into the in-house version of the finite element software FEAP98. The code is used to analyze the quasi-static test experiments and the ballistic penetration experiments.

Simulation of Quasi-Static Experiments

Numerical analyses were carried out for the quasi-static experiments and their results are compared with experimental results to verify the anisotropic visco-plastic model. Quasi-static numerical simulations were carried out to simulate off-axis tension tests and a compression test in the matrix direction under plane stress. The elastic properties, experimentally determined model parameters and other materials properties used in the plane stress analyses are given in Table 3. The rate independence exhibited by the material under quasi-static loading is simulated by taking a rate sensitivity parameters $m = 50$. A Newton-Raphson approach is used to integrate the non-linear equation of equilibrium. The tangent stiffness matrix at each iteration is computed numerically.

OFF-AXIS SIMULATIONS

Plane stress analyses of the off-axis experiments are carried out for different values of θ to verify the plasticity potential function. As shown in Figure 13, the full length of specimen, for all five fiber orientations, is discretized into 693 nodes and 310 6-noded quadratic triangular elements. The nodes at the two ends of the specimen, shown marked, are specified with zero displacement in the X-direction to simulate the gripping at the end tabs during loading in the MTS machine. Incre-

Table 3. Material properties used for plane stress quasi-static analyses.

$$C_{11} = C_{22} = 26.68 \text{ GPa}$$
$$C_{33} = 13.1 \text{ GPa}$$
$$C_{44} = C_{55} = 4.63 \text{ GPa}$$
$$C_{66} = 4.94 \text{ GPa}$$
$$C_{12} = 10.94 \text{ GPa}$$
$$C_{13} = C_{23} = 9.75 \text{ GPa}$$
$$a_{44} = 1$$
$$a_{66} = 1$$
$$m = 50$$
$$A_1 = 3.55e^{-28}, n_1 = 3.28$$
$$A_2 = 3.55e^{-55}, n_2 = 6.78$$

mental displacements are applied to end nodes in the positive and negative Y-direction, as shown in Figure 13, at the proportional rate used in the experiments. The stress and strain in the Y-direction at the strain gauge location are recorded after solution convergence for each incremental displacement. The strain gauge used in the experiments, at the center of specimen, has a dimension of 3 mm × 3 mm. As shown in Figure 13, this dimension is approximately matched in
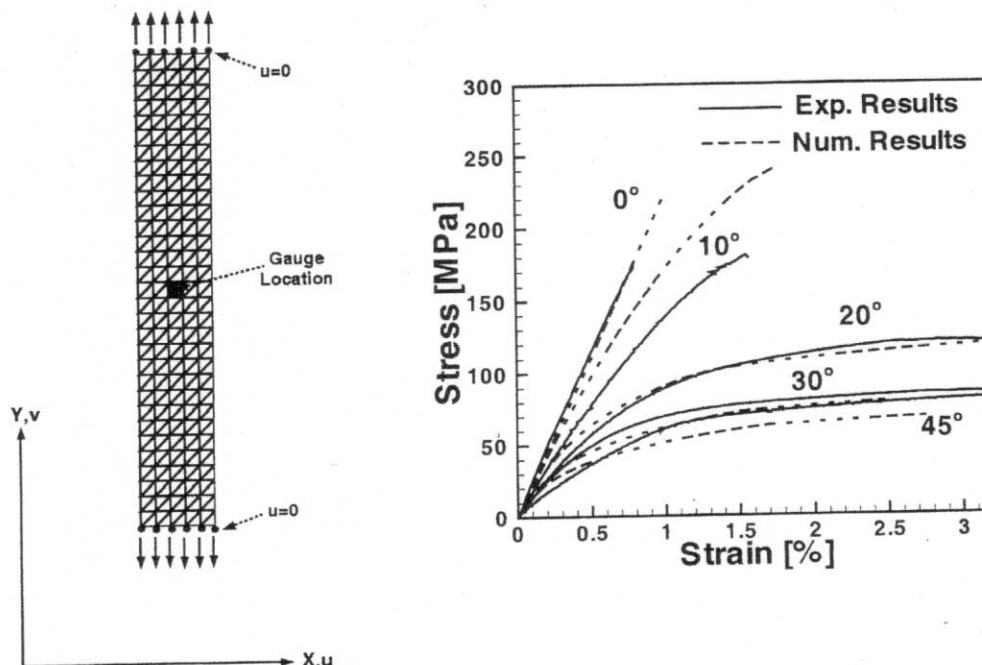

Figure 13. *Finite element mesh and comparison between FEM prediction and off-axis tension test results.*

the center by two adjacent triangular elements. The Y-direction stress and strain at the three integration points of the two elements are averaged to compare with the stress and strain at the gauge location.

Figure 13 shows the stress-strain curve obtained through analyses for the five values of θ. The experimental stress-strain curves are also shown in the figure for comparison. The figure shows that the anisotropic plasticity model predicts the material response in reasonable agreement with the experiment data except for θ = 10°. The stress-strain curve obtained from the analysis for θ = 0° matches accurately with the experimental curve. This is expected, as the response of the material is linear for the θ = 0° orientation. The model over predicts the stress for θ = 10°. However, the analysis results for higher value of θ, i.e. 20, 30, and 45°, are in better agreement with the experimental results.

COMPRESSION SIMULATIONS

Analyses were carried out to simulate the compression behavior of the GRP specimen in the direction perpendicular to the plane of the laminae and to verify the modified potential function, obtained by eliminating the S_{33} term, as discussed earlier. Due to symmetry, only a quarter of the specimen is analyzed as shown in Figure 14, with 32 six-noded triangular elements. The boundary conditions, displacement rate controlled loading at the specimen edge and the calculation of stress remain the same as given above. The material properties as given in Table 3 were used in the calculations. Figure 14 shows the stress-strain curve predicted by the modified flow potential function and its comparison with the experimental results. It is observed that the model predicts the compressive response of the GRP composite in agreement with the experimental data. It may be inferred that the
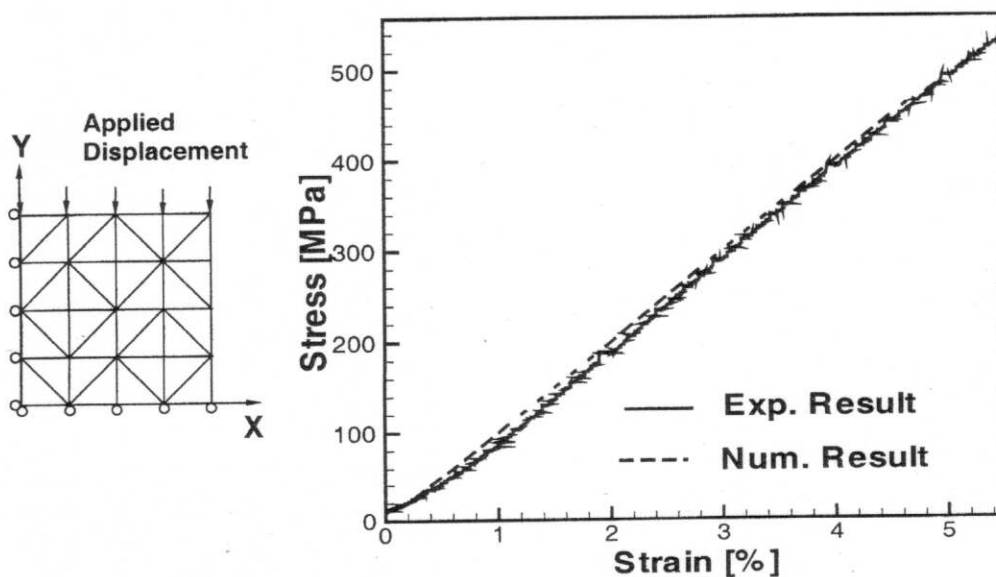

Figure 14. *Finite element mesh and comparison between FEM prediction and compression test results.*

modified potential function is appropriate for the woven GRP material considered in this investigation.

Simulation of Ballistic Penetration Experiment

As mentioned earlier, one of the important objectives in developing the visco-plasticity and contact/interface models, accounting for large displacement and rotations, interply inelasticity, and matrix delamination, is to attain the capability of simulating ballistic penetration of GRP composites, which in turn can provide insight into the role of failure mechanisms in the penetration resistance of GRP targets. In a parallel experimental activity, Espinosa et al. [4] developed a novel experimental configuration that can record projectile tail velocity histories and target back surface out-of-plane motion in penetration experiments. The configuration was used to study the ballistic penetration of the woven GRP composite plate, Espinosa et al. [4]. The experiments performed with circular rod penetrators provided information on failure mechanisms, their initiation and evolution, and their interaction. However, the precise sequence of events and stresses leading to this failure can only be identified through 3-D numerical simulations of the penetration process, due to inherent anisotropy. In order to provide an experiment that can be compared with a simple 2-D approximation, Lu [26] performed experiments using a blade-shape penetrator. Based on the planar behavior of the lamina and neglecting edge effects, the results obtained may be treated as the penetration response of GRP under 2-D plane strain condition. The integrated code is used to simulate the ballistic penetration under plane strain using advanced features of FEAP98.

The steel penetrator is modeled using a large deformation J-2 flow visco-plasticity model, Espinosa et al. [17], and each lamina of the GRP target plate is modeled using the large deformation anisotropic visco-plasticity model. Moreover, the interface between each lamina is analyzed using an interface/contact model [18]. Due to symmetry, only half of the penetrator and target are analyzed. The contact/interface properties and the material properties of steel and GRP considering plane strain are given in Table 4.

CONTACT/INTERFACE ALGORITHM

Recently, Espinosa et al. [18], proposed a multibody contact/interface algorithm to describe problems such as dynamic delamination in composite materials, discrete fragmentation of brittle materials, and analysis of material microstructures. In this case, the interface elements are embedded between laminae along their interface to analyze the cohesive interaction between the laminae. The tensile and shear tractions developed by the zero thickness interface element are calculated from the interface cohesive law. The model assumes that the interface carries forces that oppose separation and shear between two surfaces until debonding. The magnitude of these forces is a function of the relative separation and shear dis-

Table 4. Material properties for 4340 steel, GRP and interface element under plane strain conditions.

4340 Steel
Elastic Properties

E = 207 GPa	Young's modulus
ν = 0.33	Poisson's ratio
ρ_o = 8000 kg/m^3	Density
c = 5350 m/s	Longitudinal wave speed

Inelastic Properties

σ_o = 1.0 GPa	Initial yield stress
ε_o^p = 0.00483	Reference plastic strain
$\dot{\varepsilon}_o^p$ = 1000 s^{-1}	Reference plastic strain rate
α = 3	Rate sensitivity exponent
β = 5	Hardening exponent

GRP
Elastic Properties

ρ_o = 1952 kg/m^3	Density
$C_{11} = C_{22}$ = 31.55 GPa	
C_{33} = 20.0 GPa	C_{IJ} elastic anisotropic
$C_{44} = C_{55}$ = 4.63 GPa	composite material
C_{66} = 4.94 GPa	stiffness tensor
C_{12} = 15.86 GPa	in local coordinates
$C_{13} = C_{23}$ = 9.75 GPa	

Inelastic Properties

σ_o = 1.0 MPa	Initial yield stress
ε_o^p = 0.0001	Reference plastic strain
m = 100	Rate sensitivity exponent
$A_1, A_2, n_1, n_2, a_{44}, a_{66}$	See Table 3

Interface Properties

T_{max} = 50 MPa	Maximum interface stress
δ_n = 8.0 μm	Normal failure separation
δ_t = 8.0 μm	Tangent failure separation
α = 0.1	Tangential weight function
λ_c = 0.001	

placement between the two surfaces. Compressive tractions at the laminae boundaries are calculated through the impenetrability condition employed in the contact model [17,18].

The interface between two laminae is intact until the interface traction reaches a maximum value. Once the maximum traction is reached, the interface starts failing and the traction reduces to zero linearly up to a critical displacement jump, i.e., $\lambda = 1$.

In formulating the cohesive law, a non-dimensional effective displacement jump is defined by

$$\lambda = \sqrt{\left(\frac{u_n}{\delta_n}\right)^2 + \beta^2 \left(\frac{u_t}{\delta_t}\right)^2} \tag{35}$$

where, u_n and u_t are the actual normal and tangential displacement jumps at the interface estimated by the finite element analysis, and δ_n and δ_t are critical values at which interface failure takes place.

For a triangular $T - \lambda$ law, for loading and unloading in the range $0 \le \lambda \le \lambda_{cr}$

$$T_n = \frac{u_n}{\delta_n} \frac{T_{max}}{\lambda_{cr}}; T_t = \alpha \frac{u_t}{\delta_t} \frac{T_{max}}{\lambda_{cr}} \tag{36}$$

where T_{max} is the maximum normal traction which the interface can develop before failure and $\alpha = \beta^2(\delta_n/\delta_t)$ is the parameter coupling the normal and shear tractions, such that $\beta^2 = G_{IIc}/G_{Ic}$.

It is assumed here that the traction can increase reversible and linearly to its maximum value $T = T_{max}$ when $\lambda = \lambda_{cr}$. Beyond λ_{cr}, the traction reduces to zero up to $\lambda = 1.0$ and any unloading takes place irreversibly.

For loading in the range $\lambda_{cr} < \lambda \le 1$;

$$T_n = T_{max} \frac{u_n}{\delta_n} \frac{1-\lambda}{\lambda(1-\lambda_{cr})}; T_t = \alpha T_{max} \frac{u_t}{\delta_t} \frac{1-\lambda}{\lambda(1-\lambda_{cr})} \tag{37}$$

Due to irreversibility, loading/unloading in the range $0 \le \lambda \le \lambda*$, where $\lambda* > \lambda_{cr}$ is the last value of λ from where unloading took place, is given by

$$T_n = T_{max} \frac{u_n}{\delta_n} \frac{1-\lambda*}{\lambda*(1-\lambda_{cr})}; T_t = \alpha T_{max} \frac{u_t}{\delta_t} \frac{1-\lambda*}{\lambda*(1-\lambda_{cr})} \tag{38}$$

For loading in the range $\lambda* < \lambda \le 1$;

$$T_n = T_{max} \frac{u_n}{\delta_n} \frac{1-\lambda}{\lambda(1-\lambda_{cr})}; T_t = \alpha T_{max} \frac{u_t}{\delta_t} \frac{1-\lambda}{\lambda(1-\lambda_{cr})} \tag{39}$$

Once the actual displacement jump exceeds a specified critical value, the interface elements are assumed to have failed and microcracking is said to have initiated at that interface. Subsequent failure of neighboring interface elements leads to delamination (see Figure 15).

ADAPTIVE REMESHING

Element distortion inside the laminae as the penetrator advances can reduce the stable time step of the explicit time integrator to a point where the computation no longer advances and the field variables are not accurately interpolated. A solution to this problem is to rediscretize the domain with a new, undistorted mesh, and continue with the calculation. Adaptive mesh optimization together with a mesh transfer operator was used for that purpose. This technique consists mainly in an optimization problem where the aim is to improve the quality of the mesh performing certain operations over the mesh. The objective function in this case would be the quality of the elements Q_k, where their shapes and sizes are evaluated depending on the desired size and shape that the mesh requires, viz.,

$$Q_k = \alpha V_k / P_k * \exp[-\beta^2 \log^2(h_k / h^*)] \tag{40}$$

where V_k is the area, P_k is the perimeter, in this case $h_k = P_k/3$, h^* is the desired size of element k and α and β are fixed parameters [27,28]. It is useful to introduce more elements in those regions of the mesh that are rapidly deforming. This decision is based on the rate of plastic work, $\dot{W}^p = \sigma \dot{\varepsilon}^p$ [17,29]. A summary of this procedure is given in Table 5.

Typically, user defined values are: $\dot{W}^p_{min} = 0.1$, $\dot{W}^p_{max} = 1.5$, $\Delta h_{ref} = 0.2$, $\Delta h_{coar} = 2.0$, finally $h_{min} = 0.2$ mm and $h_{max} = 1.0$ mm which are given by the dimension of the problem.
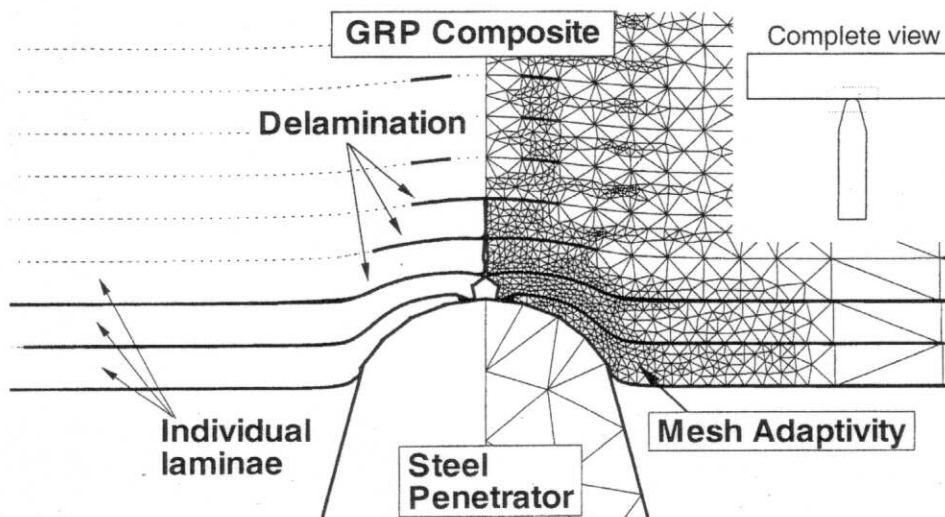

Figure 15. *Schematics of composite delamination and mesh adaptivity.*

Table 5. Refinement/coarsening algorithm.

Input: $\dot{W}^p_{min}, \dot{W}^p_{max}, h_{min}, h_{max}, \Delta h_{ref}, \Delta h_{coar}$ (User defined parameters)

Evaluate $\dot{W}^p_{av}$ (Averaged rate of plastic work of the body)

Loop over elements.

- For each element, e, evaluate $\dot{W}^p_e$, (rate of plastic work) and size h.

- IF $\left(\dfrac{\dot{W}^p_e}{\dot{W}^p_{av}} < \dot{W}^p_{min} \right)$ (Then $\Rightarrow$ **COARSENING**)

   $- h^* = h * \Delta h_{coar}$

   $-$ IF ($h^* > h_{max}$) Then $h^* = h_{max}$

- ELSE IF $\left(\dfrac{\dot{W}^p_e}{\dot{W}^p_{av}} > \dot{W}^p_{max} \right)$ (Then $\Rightarrow$ **REFINEMENT**)

   $- h^* = h * \Delta h_{ref}$

   $-$ IF ($h^* < h_{min}$) Then $h^* = h_{min}$

- ELSE $\Rightarrow$ NOTHING

Perform Adaptive Remeshing

The quality of the mesh τ is defined as $Q_\tau = \min Q_k, k \in \tau$. If $\bar{k}$ is the worst element in the mesh (i.e., $Q_{\bar{k}} \leq Q_k \ \forall \ k$), at each *iteration* the submesh formed by $\bar{k}$ and its neighbors (elements sharing a node or an edge with $\bar{k}$) is considered. On this submesh, several operations are *virtually* performed, until one is found to yield a better quality. This operation is then *really* performed. The operations consist in defining a *cluster*, removing its interior node, and either connecting all the edges in the cluster boundary to one of the boundary nodes or connecting them to a node at the center of the cluster. Two types of clusters are considered, *edge* clusters are all elements that share some given edge, and *nodal* clusters are all elements that share some given node [see Figure 16 (a)]. These operations have been taken from Coupez's method [30] and they have been used by Buscaglia and Dari [28] as an anisotropic mesh adaptivity method.

Although this kind of optimization technique, which is called *topological* mesh optimization, improves the shape of the elements, it does not allow the nodes to move, and it is highly possible that some elements will end up deformed.

A node-movement optimization algorithm (also called *geometrical* mesh optimization) has been implemented. The objective function Q_{global} is maximized over the space of nodal locations. Since the simultaneous optimization of the locations of all the nodes in a mesh consisting of thousands of elements is obviously intractable, only the position of those nodes that belong to the worst element of the mesh, and their nth-order neighbors (with $n = 1$ or 2) are modified. Since the min functions are non-differentiable this algorithm is based on a *node-by-node* discrete op-
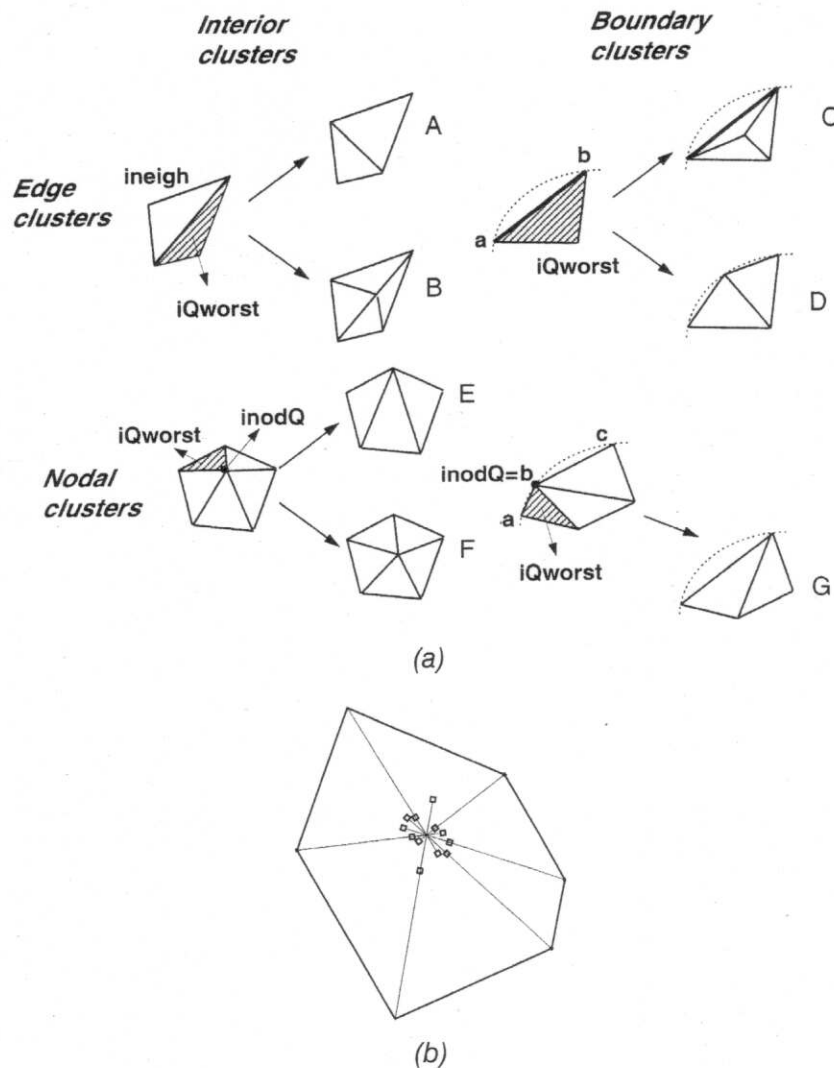
(a)

(b)

Figure 16. *(a) Operations allowed in the* topological *mesh optimization algorithm. iQworst is the element with the worst quality. For the case of nodal cluster, inodQ is the node that represents the cluster. (b) Local geometrical optimization, the node is relocated in different positions until the cluster or submesh reaches the best quality.*

timization method. The optimization is performed independently in each node and the objective function Q_{global} is the quality of the *submesh* formed by the elements that share that node. The quality is evaluated for different positions (or *sampling positions*) of the node until it reaches the maximum [see Figure 16 (b)]. A detailed description of this *geometrical* mesh optimization algorithm can be found in References [17,31].

MESH TRANSFER OPERATOR

Once the mesh is adapted, the solution needs to be transferred from the old mesh to the new one. This is achieved with the *mesh transfer operator* presented by Espinosa et al. [17], which addresses the issues of requirements of static or dy-

namic equilibrium, consistency with the constitutive equations, compatibility of the state transfer with the displacement field on the new mesh, compatibility with evolving boundary conditions and minimization of numerical diffusion of state variables.

Update of configuration: The model uses a Lagrangian formulation. If a mesh is rebuilt, but the reference configuration is *not* updated, the distortion merely changes its location from the current configuration to that of the reference. To truly remove the distortion, the reference configuration must be periodically moved forward to the current configuration. The reference configuration is defined as the configuration at which the displacements are zero. So part of updating the reference configuration is setting

$$\hat{\mathbf{x}} = \mathbf{X} + \mathbf{u} \tag{41}$$

$$\hat{\mathbf{u}} = 0 \tag{42}$$

$$\mathbf{x} = \hat{\mathbf{x}} + \hat{\mathbf{u}} \tag{43}$$

wherein $\mathbf{X}$, $\mathbf{u}$, $\hat{\mathbf{x}}$, and $\hat{\mathbf{u}}$ are the reference particle positions and displacements in the old and new reference configurations, respectively. The deformation gradient relates the current configuration to the reference configuration by $\mathbf{F} = \partial \mathbf{x} / \partial \mathbf{X}$.

However, when the reference configuration is updated, the relation becomes slightly more complicated. After an update, the deformation gradient expands to

$$\mathbf{F}^{old} = \mathbf{I} + \frac{\partial \mathbf{u}}{\partial \mathbf{X}} \tag{44}$$

$$\mathbf{F} = \left(\mathbf{I} + \frac{\partial \hat{\mathbf{u}}}{\partial \hat{\mathbf{X}}} \right) \mathbf{F}^{old} \tag{45}$$

Transfer of variables: State variables in the new mesh are subdivided into two sets, interpolated and computed variables, see Table 6. For the interpolated set, the state variables are interpolated in the deformed configuration based upon shape functions of an auxiliary element connectivity of simple 3-node triangles connecting all of the existing nodes in the old mesh. This sort of interpolation is conducted for the nodal kinematic quantities as well as for the components of the stress tensor $\mathbf{S}$ and the internal variables $\overline{\mathbf{Q}}$ using an auxiliary mesh obtained by 3-node triangular elements connecting quadrature points in the old mesh [17].

It should be noted that not all of the variables may be interpolated. If everything would be interpolated, the stress state after the mesh update would be inconsistent with the state of displacement. The problem then requires a suitable choice of field variables to be interpolated and other field variables to be computed to keep the solution stable and consistent with the equations of motion and the material constitutive equations. The deformation gradient $\mathbf{F}$ is obtained directly from the interpo-

Table 6. Interpolated and computed state variables.

Set of interpolated variables: $I(u, v, a, \bar{E}^p_{int}, \bar{\bar{E}}^p_{int}, S^{int})$
Set of computed variables: $C(F, \bar{S}_y, S^{corr})$

lated displacement **u**. For the interpolated second Piola-Kirchhoff stress tensor $\mathbf{S}^{int}$ some corrections need to be made in order to preserve the strain rate. Table 7 gives a summary of those corrections.

Another technique is implemented which allows the nodes on the axis of symmetry to separate after they reach the maximum tensile strength of the glass fiber, approximately 1 GPa. Figure 15 describes the mechanisms implemented in the code to simulate GRP ballistic penetration. In general, the laminae start breaking at the impacted face, adaptive remeshing occurs only in the GRP target starting with the first lamina and continues with the other laminae as the penetrator advances. In most cases, mesh refinement does not occur in the penetrator what indicates that there is no plastic deformation in the steel.

NUMERICAL SIMULATIONS

In order to make a comparative and systematic study of ballistic penetration, five cases are analyzed. In the first four cases, an anisotropic *visco-plastic* model is used for GRP, assuming the plate to constitute 1, 10, 20 and 40 laminae respectively, as shown in Figure 17. In the last case, GRP plate with 40 laminae is analyzed using an anisotropic *elastic* model. In this way, we can analyze whether or not visco-plasticity and delamination play an important role as absorption energy mechanisms.

Table 7. Flowchart for the calculation of variables in set C from the interpolated set I.

$$\bar{S}_y = \left(\frac{\bar{E}^p_{int}}{A} \right)^{1/n}$$

$$\downarrow$$

$$factor = \left(\frac{\bar{\bar{E}}^p_{int}}{\bar{\bar{E}}^p_0} \right)^{1/m} \frac{\bar{S}_y}{\bar{S}} \rightarrow S^{corr}_{ij} = S^{int}_{ij} \times factor$$

$$\uparrow$$
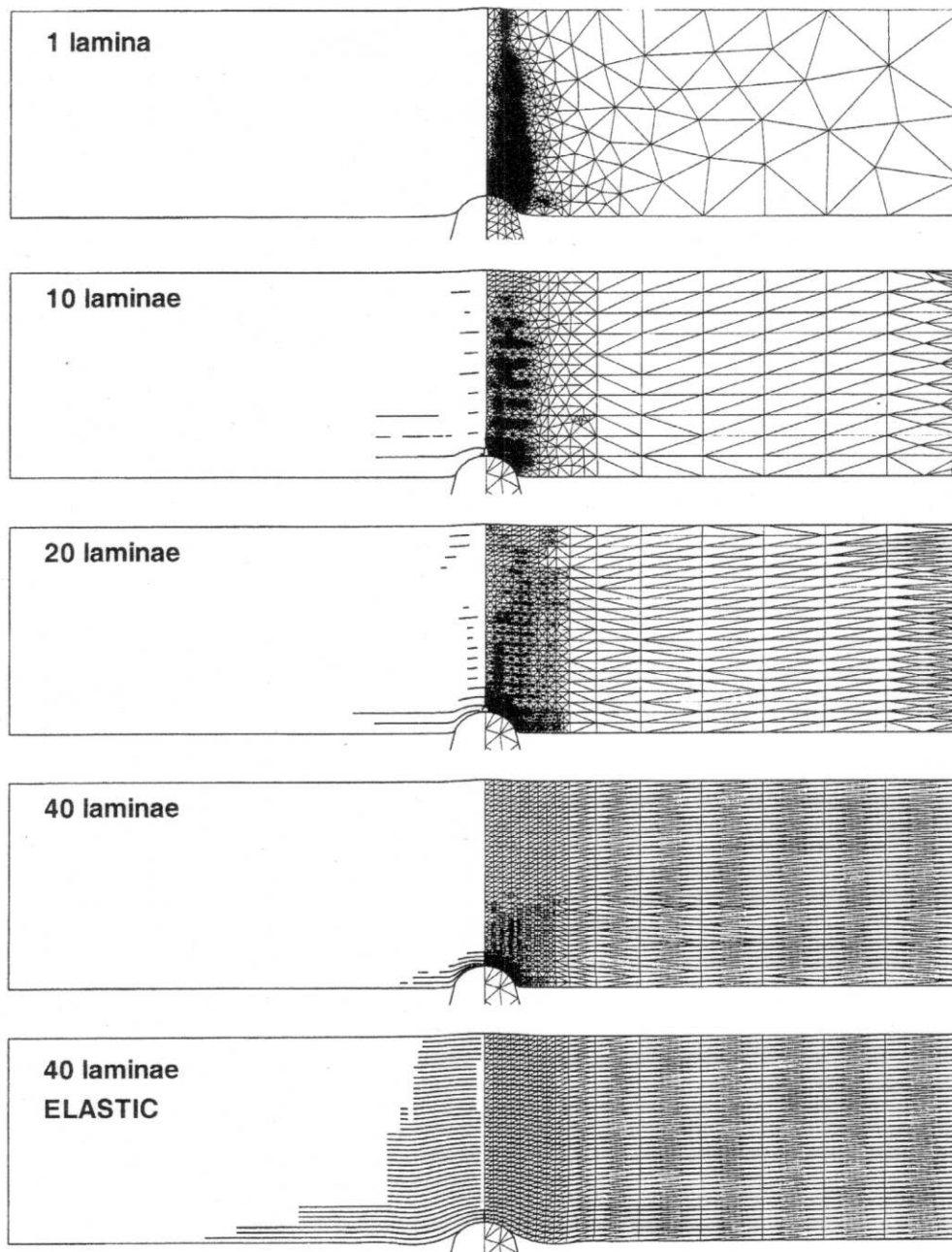
$$\bar{S} = \sqrt{3f(S^{int}_{ij})}$$

Figure 17. Plane strain 1, 10, 20 and 40 laminae simulation FEM mesh employed in the ballistic penetration simulations using the anisotropic visco-plastic model. The fifth mesh represents the simulations that use 40 laminae using an anisotropic elastic model.

In some cases the analyses terminated at early stages of the calculation (about 15 μsec) due to element distortion. Figure 15 clearly shows how the elements of the first lamina are likely to suffer severe distortion as the penetrator advances and the first lamina loses its thickness. These conditions become worse as the number of laminae increases. Even though the mesh adaptivity technique implemented is based on the state of plastic deformation of the element, the key point of this algorithm is finding the moment when the calculation becomes inefficient using the old mesh to require a new mesh. Based on the relationship between the time step and the maximum frequency of the mesh, the condition currently in use compares the current time step to a reference value set at the end of the previous remeshing. In this way, if the time step drops, meaning that at least one of the elements is distorting, the remeshing is triggered.

During the ballistic penetration experiments, the particle velocity at the back surface of the GRP target was recorded for comparison with numerical simulation results [26,4]. Figure 18(a) presents the velocity profile obtained using the anisotropic visco-plastic model with 10, 20, and 40 laminae versus the experimental result [26]. The analyses predict a 60 m/sec higher peak velocity value. However, the velocity reduces sharply after the peak value is reached.

Figure 18(b) compares the velocity profile obtained using anisotropic elastic model with 40 laminae with the velocity profile obtained using visco-plastic model with 1 lamina and 20 laminae depicting visco-plasticity and delamination. The velocity profile for the elastic case is shaped by the arrival of an initial compression pulse reaching the maximum velocity of 320 m/sec in 20 μsec, followed by a velocity reduction caused by the separation of central nodes and delamination, see Figure 17. Comparing the results for one lamina with the case with 20 laminae, the later dissipates additional energy through delamination, resulting in a reduction of the velocity jump from 160 m/sec to 100 m/sec.

For a better understanding of the energy absorption phenomenon, modes of energy dissipation are analyzed for each case. The variation in time of the total internal energy, defined as the sum of elastic and visco-plastic internal energy, is plotted in Figure 19(a). For the calculation with one lamina target without interface elements, internal energy stored in the target plates is maximum. For multi-lamina analyses with interface elements, delamination dissipates total energy reducing the internal energy stored in the target. Even though the internal energy stored in the penetrator is significantly smaller than the internal energy stored in the target, their behaviors are similar.

The kinetic energy of the target [Figure 19(b)] does not show much difference for 10, 20, 40 laminae compared with the case with one lamina, which explains the similarity in the velocity profiles (Figure 18).

Figure 20(a) in comparison with Figure 19(a) shows that a significant amount of internal energy is due to the plastic deformation of the GRP laminae. As the number of laminae increases, the plastic deformation localizes first in few laminae ab-
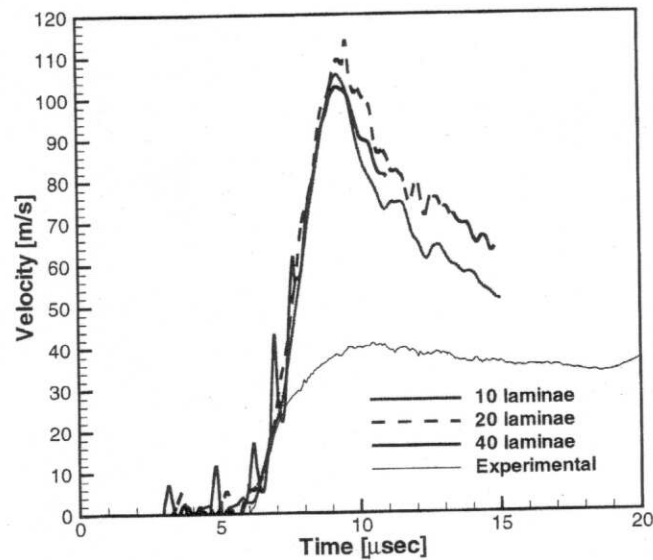
(a)
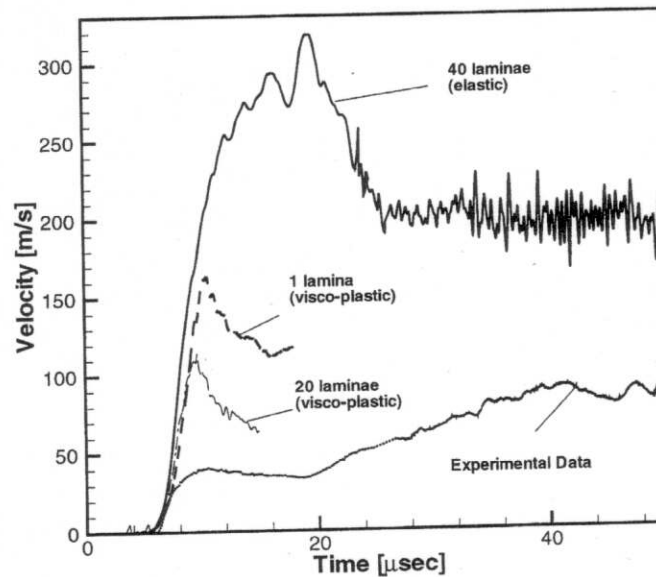
(b)

Figure 18. *(a) Velocity profiles of 10, 20 and 40 laminae, with GRP visco-plasticity model . (b) Velocity profiles of delamination study for 40 laminae with elasticity, the case with one lamina and visco-plasticity in comparison with a multi-laminae case with visco-plasticity..*

sorbing less plastic internal energy than in the cases with a smaller number of laminae per unit thickness. As expected, the delamination energy increases as the number of laminae is increased as shown in Figure 20(b).

Another point worth mentioning is the fact that the velocity profile is dependent on the distance from the target center. It is observed that the velocity decreases significantly when the observation point is moved laterally. This feature is important because experimental errors of 2-3 mm in the location of the laser beam are possible, providing a possible explanation for the discrepancy seen in Figure 21.
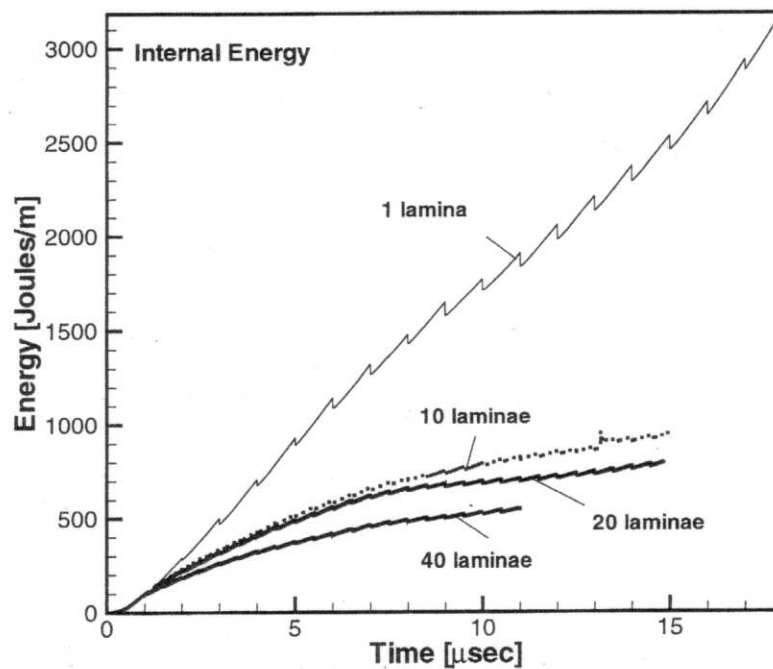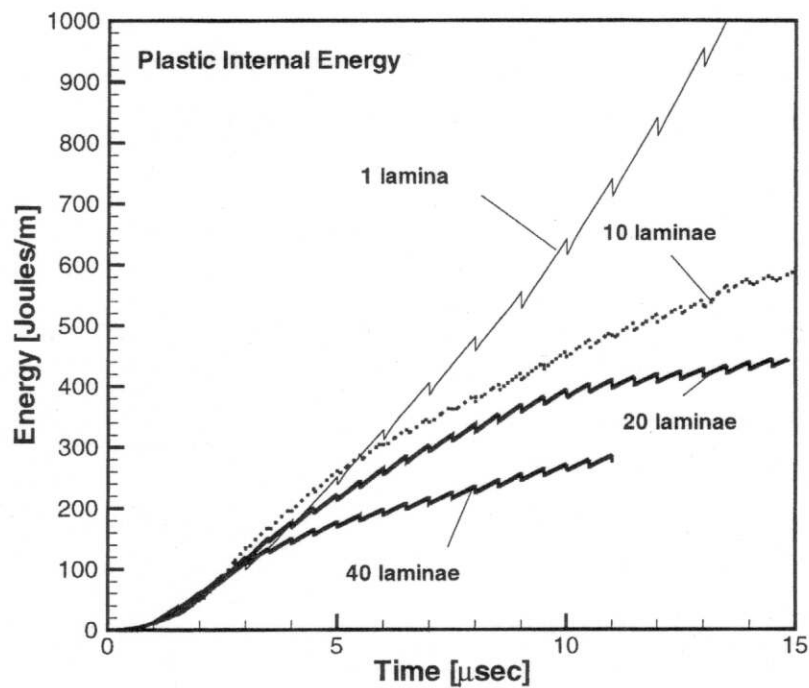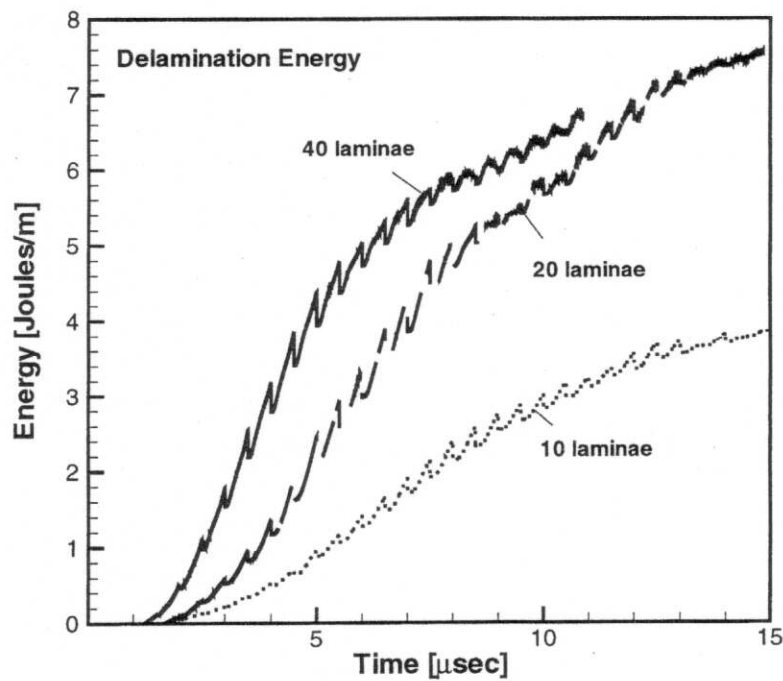
(a)
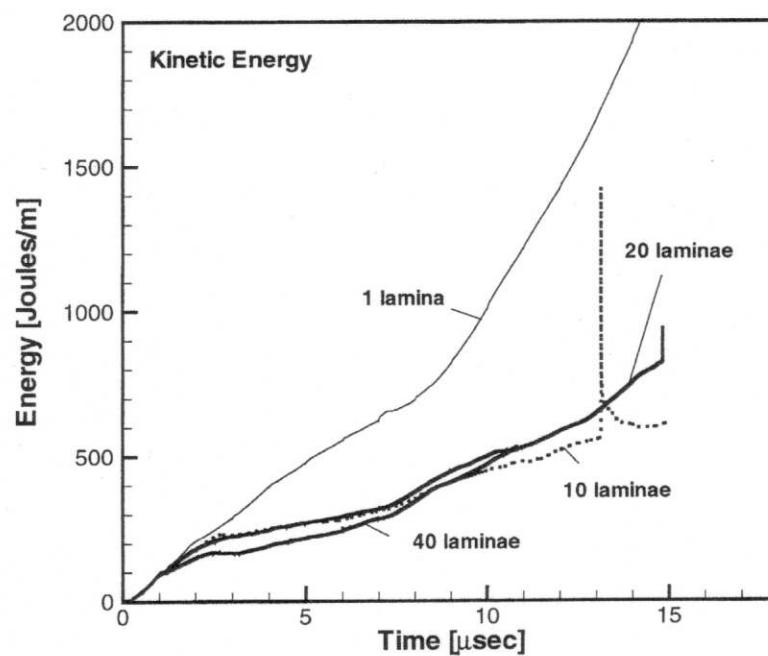
(b)

Figure 19. (a) Internal energy profiles for 1, 10, 20 and 40 laminae. (b) Kinetic energy profiles
of GRP plate target for 1, 10, 20 and 40 laminae.

(a)

(b)

Figure 20. *(a) Plastic energy profiles of target for 1, 10, 20 and 40 laminae. (b) Delamination energy profiles for 10, 20 and 40 laminae.*
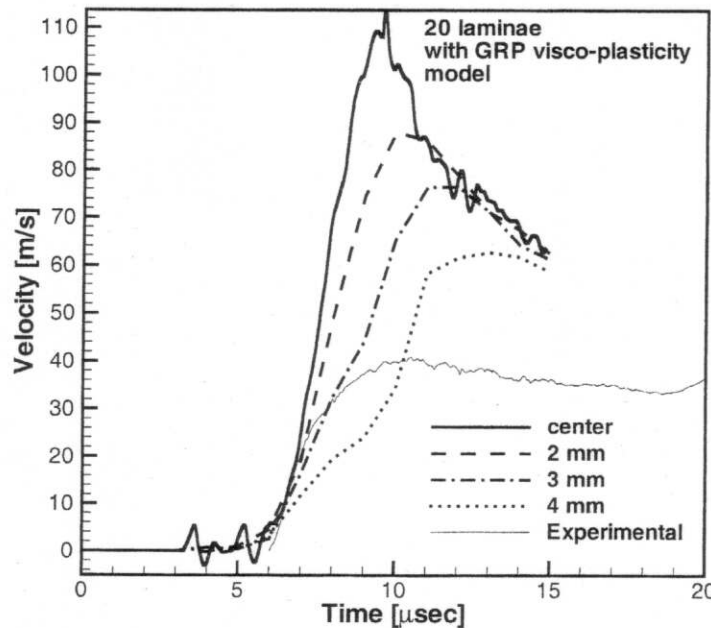
Figure 21. *Velocity histories at the target center and locations 2, 3 and 4 mm from symmetrical axis.*

CONCLUDING REMARKS

A general 3-D finite deformation anisotropic visco-plasticity model for GRP composites is presented in total Lagrangian co-ordinates. The plastic potential of the composite materials is described through a quadratic stress function. The parameters of the anisotropic constitutive model are determined by off-axis tension, compression, and Arcan's shear tests. The model takes into account the temperature and strain rate dependence into the visco-plastic deformation.

The various tests carried out to determine the parameters of the visco-plastic model have exhibited many complex behaviors of woven GRP composite after first failure and need further exploration. However, as mentioned earlier, the present homogenized model finds the response of the material up to the onset of material instability. The analysis in the post-failure regime needs to be carried out using additional techniques, e.g., models accounting for fiber buckling. Hence, the model parameters derived from the test results are adequate to simulate the overall continuum deformation of FRP composites.

The off-axis tension tests show that the woven GRP composite, considered in the present work behaves linearly until failure when the load is applied along the fiber direction. The visco-plasticity exhibited by the material in the plane of the lamina increases with the increase of the angle between the fiber and loading direction. Also, during off-axis loading, the material exhibits nonlinear behavior from the beginning of the loading. Hence, the visco-plastic behavior of GRP material is contributed mainly by the visco-plasticity in the polymer matrix. Neverthe-

less, the off-axis tension/compression tests allow the derivation of a master effective stress–effective plastic strain curve which is highly suitable for numerical simulations. The master curve so obtained is described by a set of two power laws in order to characterize the plastic behavior of the composite from the onset of loading. Separate power laws can be used to describe loading and unloading to fit the master curve. The off-axis compression tests, with $\theta = 45°$, show that the material behaves identically in tension and compression. These features allow the formulation of a visco-plastic model in the effective stress–effective strain space.

When compression tests are performed along the fiber direction, material instabilities are observed. The stress relaxation observed during these experiments is due to delamination and fiber buckling. However, buckling is not easily incorporated in a homogenized visco-plasticity model. Such material instabilities need a separate treatment, which are not the focus of this paper. However, as observed for $\theta = 45°$, the instability vanishes as the plastic flow creeps in due to enhanced participation of the matrix materials at higher value of θ. Hence, neglecting the instabilities, the woven GRP material behaves identically in tension and compression.

The compression test further reveals that the woven composite has a linear behavior until failure when loaded normal to the plane of the lamina. This observation has allowed the term S_{33} to be neglected in the plastic flow potential function. This simplification, based only on the compression tests results, is appropriate due to limited strength of the composite materials in tension along the thickness direction. For example, compared with the compressive strength of over 500 MPa determined here, the delamination tensile stress of the composite is 30–50 MPa [32]. Hence, the modified plastic potential appears appropriate to describe the large deformation of the woven GRP composite under general loading.

The material shows a very limited strength of about 3 MPa in out-of-plane pure shear as obtained by tests performed with Arcan's shear fixture. It should be mentioned again that out-of-plane shear experiments performed with Arcan's shear fixture are highly delicate due to the limited strength of the material in shear and bending. A slight eccentricity or bending of the specimen, during the experiment, causes faulty readings or even breakage of the GRP specimen. The experimental results given here are few out of several unsuccessful attempts in this regard. Great care was required to conduct the experiment successfully. It has to be emphasized that a combined loading test involving all the stress components present in the flow potential needs to be conducted to verify the model parameters obtained through the off-axis and shear tests. Unfortunately, such tests require a very complex loading device. For this reason, it has not been pursued in this work and remains one of the core objectives of future research work.

Depending on the matrix material, other functional forms for describing the ply inelasticity may be needed, e.g., visco-elastic representation would also be feasible. For the purpose of simulating ballistic penetration of GRP composites, it has been assumed in the present work that a visco-plastic description can adequately

capture the GRP material response in a macroscopic sense, i.e., plies inelasticity (matrix cracking, fiber debonding, matrix inelasticity) is represented by the model here described, while interply delamination is modeled by means of cohesive/contact laws.

The anisotropic visco-plasticity model has been integrated with the in-house version of the finite element code FEAP98. The analyses carried out for the off-axis tension tests and compression tests show that the model is able to predict the GRP response in confirmation with the experiments. The integrated model has subsequently been used to study dynamic delamination in woven GRP composite [18]. The simulations are very much in agreement with the available plate impact experimental data.

The finite deformation anisotropic plasticity model is used with the interface/contact model and mesh adaptivity to study energy dissipation during ballistic penetration of the GRP plate. The simulations with 10, 20 and 40 laminae show a reasonable agreement with the profile obtained experimentally. Compared with the elastic analysis with no interface elements, anisotropic visco-plasticity model with delamination and mesh adaptivity presented the best agreement with the experimental velocity history. The difference observed between the simulation results and the experimental results still presents the necessity of modeling additional failure mechanisms and wave dispersion. It is known that GRP materials have a layered composition within each ply, see Reference [18]. As a result, significant wave dispersion is observed in plate impact experiments, see Espinosa et al. [18]. In the present analyses, wave dispersion resulting from material heterogeneity was not accounted for. Future research should address this feature within the framework of continuum homogenized models.

Mesh adaptivity for this kind of simulation is still a challenge and further improvements are necessary to resolve the early termination of some calculations. Since the time step is not directly connected with the spatial coordinates, remeshing should be done when the error due to spatial discretization becomes highly significant. Several approaches are possible, the use of error estimates based on error norms on stresses or strains computed in the finite element mesh, or the use of distortion criteria characterizing the geometrical deformation of the element.

The finite deformation anisotropic visco-plastic model, presented here, can be used for any unidirectional or bidirectional fiber reinforced composite material. The model parameters in the visco-plastic potential function need to be determined for the particular material under consideration. Our experiments have shown that the material is in-sensitive to strain rate in the loading range of 0.001 mm/s to 0.1 mm/s. Efforts are currently afoot to carry out experiments with a Kolsky bar to study the material rate dependence in the strain rate range 100–1000/sec which is generally encountered during impact and penetration. Out-of-plane plate impact shear tests, at strain rates of the order of 10^5/sec, were

performed by Espinosa et al. [33]. Similarly, additional work is required to assess temperature effects on the material visco-plastic response.

It is expected that the proposed model and the dynamic delamination model discussed in Espinosa et al. [18] would provide a valuable computational tool for the analysis of inelasticity of fiber composites used in automotive, aerospace and defense industries.

ACKNOWLEDGMENTS

REFERENCES

1. Cantwell, W. and Morton, J. 1991. Composites, 22(5):347–362.
2. Abrate, S. 1991. Trans. American Society of Mechanical Engineers; Applied Mechanics Review, 44(4):155–190.
3. Abrate, S. 1994. Trans. American Society of Mechanical Engineers; Applied Mechanics Review, 47(11):517–544.
4. Espinosa, H., Lu, H.-C. and Xu, Y. 1996. Journal of Composite Materials, 32:722–743.
5. Sun, C. and Chen, J. 1989. Journal of Composite Materials, 23:1009–1020.
6. Hill, R. 1950. The Mathematical Theory of Plasticity. Oxford University Press.
7. Chen, F. and Sun, C. 1997. Journal of Composite Materials, 31(8):788–811.
8. O'Donoghue, P., Anderson (Jr.), C., Friesenhahn, G. and Parr, C. 1992. 26(13):1860–1884.
9. Voyiadjis, G. and Thiagarajan, G. 1995. International Journal of Plasticity, 11:867–894.
10. Voyiadjis, G. and Thiagarajan, G. 1996. International Journal of Plasticity, 12(1):69–91.
11. Aboudi, J. 1989. Applied Mechanics Reviews, 42:193–221.
12. Paley, M. and Aboudi, J. 1992. Mechanics of Materials, 14:127–139.
13. Stout, M., Liu, C. and Haberman, K. S. 1998. Experimental Mechanics, Allison (ed.); Balkema, pp. 187–192.
14. Hsiao, H. and Daniel, I. 1996. Composites A, 27:931–941.
15. Hsiao, H. and Daniel, I. 1996. Journal of Engineering Materials and Technology, 118:561–570.
16. Hsiao, H. and Daniel, I. 1996. Composites Science and Technology, 56:581–593.
17. Espinosa, H., Zavattieri, P. and Emore, G. 1998. In Espinosa, H. and Clifton, R., editors, Special Issue of Mechanics of Materials, 29:275–305.
18. Espinosa, H., Dwivedi, S. and Lu, H.-C. 2000. Computer Methods in Applied Mechanics and Engineering, 183(3): 259–290.
19. Bathe, K. J. 1996. Finite Element Procedures. Prentice Hall.

20. Cook, R. D. 1974. Concepts and Applications of Finite Element Analysis. John Wiley and Sons Inc., New York.

21. Arcan, M., Hashin, Z. and Voloshin, A. 1978. Experimental Mechanics, 18:141–146.

22. Voloshin, A. and Arcan, M. 1979. Journal of Composite Materials, 13:240–246.

23. Voloshin, A. and Arcan, M. 1980. Experimental Mechanics, 280–284.

24. Aravot, Y., Arcon, L., Arcon, M. and Albu-Yaron, A. 1990. Journal of Materials Science, 25:3714–3722.

25. Chou, S.-C. and Deluca, E. 1993. Report number ARL-SR-5; Army Research Laboratory; Aberdeen Proving Ground; USA.

26. Lu, H.-C. 1998. Ph.D. thesis, Purdue University, West Lafayette, IN.

27. Zavattieri, P., Dari, E. A. and G. C., B. 1996. Int. J. Numer. Meth. in Engng., 39:2055–2071.

28. Buscaglia, G. and Dari, E. 1997. Int. J. Numer. Meth. Engng., 40:4119–4136.

29. Zavattieri, P. 1999. Ph.D. thesis, Purdue University, West Lafayette, IN.

30. Coupez, T. 1994. In Weatherill, N. et al., editor, Numerical Grid Generation in Computational Fluid Dynamics and Related Fields, pp. 615–625. Pineridge Press, Swansea.

31. Zavattieri, P., Buscaglia, G. and Dari, E. 1996. Latin American Applied Research, 26:233–236.

32. Dandekar, D. and Beaulieu, P. 1995. AD-Vol., 48.

33. Espinosa, H., Lu, H.-C. and Xu, Y. 1997. Acta Materialia, 45(11):4855–4865.